

EVOLUTION OF MIGRATING PLANETS UNDERGOING GAS ACCRETION[†]

GENNARO D'ANGELO¹

NASA Ames Research Center, Space Science and Astrobiology Division, MS 245-3, Moffett Field, CA 94035

AND

STEPHEN H. LUBOW

Space Telescope Science Institute, 3700 San Martin Drive, Baltimore, MD 21218

July 16, 2008

ABSTRACT

We analyze the orbital and mass evolution of planets that undergo run-away gas accretion by means of two- and three-dimensional hydrodynamic simulations. The disk torque distribution per unit disk mass as a function of radius provides an important diagnostic for the nature of the disk-planet interactions. We first consider torque distributions for nonmigrating planets of fixed mass and show that there is general agreement with the expectations of resonance theory. We then present results of simulations for mass-gaining, migrating planets. For planets with an initial mass of 5 Earth masses (M_E), which are embedded in disks with standard parameters and which undergo run-away gas accretion to one Jupiter mass (M_J), the torque distributions per unit disk mass are largely unaffected by migration and accretion for a given planet mass. The migration rates for these planets are in agreement with the predictions of the standard theory for planet migration (Type I and Type II migration). The planet mass growth occurs through gas capture within the planet's Bondi radius at lower planet masses, the Hill radius at intermediate planet masses, and through reduced accretion at higher planet masses due to gap formation. During run-away mass growth, a planet migrates inwards by only about 20% in radius before achieving a mass of $\sim 1 M_J$. For the above models, we find no evidence of fast migration driven by coorbital torques, known as Type III migration. We do find evidence of Type III migration for a fixed mass planet of Saturn's mass that is immersed in a cold and massive disk. In this case the planet migration is assumed to begin before gap formation completes. The migration is understood through a model in which the torque is due to an asymmetry in density between trapped gas on the leading side of the planet and ambient gas on the trailing side of the planet.

Subject headings: accretion, accretion disks — hydrodynamics — methods: numerical — planetary systems: formation — planetary systems: protoplanetary disks — solar system: formation

1. INTRODUCTION

In the core accretion picture of planet formation (Bodenheimer & Pollack 1986; Wuchterl 1991; Pollack et al. 1996; Hubickyj et al. 2005, and references therein), a small mass solid core initially rapidly accretes solid material, followed by a slow evolution phase of gas and solid accretion. During this slow evolution phase, the planet is limited in its ability to accrete gas by the thermal heating caused by the impacting solids. Once the planet's gas mass is greater than its solid mass, typically at several Earth masses, the planet undergoes “run-away” gas accretion, in which it can accrete whatever mass is provided to it. These processes have been treated by one-dimensional, spherically symmetric structure calculations in the above papers.

On the other hand, multi-dimensional hydrodynamical calculations of a protostellar disk interacting with the planet has revealed various flow properties of the gas, including the gap opening by tidal effects, previously anticipated by one-dimensional disk models (Lin

& Papaloizou 1986). In addition, planet migration that results from disk-planet interactions has been analyzed by means of such simulations. Good agreement is often, but not always, found between the simulations and the expectations of theory (Nelson et al. 2000; Bate et al. 2003; D'Angelo et al. 2003; Nelson & Benz 2003; Li et al. 2005; D'Angelo et al. 2006). These calculations typically do not include the mass evolution of the planet. Usually they apply accretion boundary conditions onto the planet as a means of modelling the run-away gas accretion process. One aim of this paper is to analyze the effects of planet mass growth on migration.

Several controversies remain on the effects of gas. The role of coorbital torques on planet migration, in the sub-giant mass range, is not well understood. Masset & Papaloizou (2003, hereafter MP03) suggested on the basis of a model and simulations that a fast mode of migration (sometimes called Type III migration) can occur due to strong coorbital torques. Ogilvie & Lubow (2006, hereafter OL06) found support for the concept of coorbital dominated migration under certain conditions. At higher grid resolution under the conditions specified by MP03, simulations by D'Angelo et al. (2005, hereafter DBL05) found that the migration rate was much slower.

Another subject of interest is how planet masses may be limited by a reduction in the gas accretion rate. Lin

Electronic address: gennaro.dangelo@nasa.gov

Electronic address: lubow@stsci.edu

¹ NASA Postdoctoral Fellow.

[†] To appear in THE ASTROPHYSICAL JOURNAL (v684 n1 September 20, 2008 issue). Also available as ApJ preprint doi: 10.1086/590904 and as ARXIV preprint: [arXiv:0806.1771](https://arxiv.org/abs/0806.1771).

& Papaloizou (1986) proposed such a reduction by tidal torques that open a gap about the orbit of the planet. The value of the highest planet mass achieved in the presence of gap opening is somewhat controversial. Some studies (Lubow et al. 1999; Bate et al. 2003; D'Angelo et al. 2003) have suggested that the maximum planet mass is about 6–10 M_J , corresponding to the upper limit of the observed range of extrasolar planets (Marcy et al. 2005; Butler et al. 2006). This limit suggests that some other process, such as disk dispersal or other self-limiting feedback on planetary accretion, is responsible for the lower masses ($\sim 1 M_J$) typically found observationally. Other studies suggest that the tidal limit is $\sim 1 M_J$ and therefore no additional process is required to explain the typical masses (e.g., Dobbs-Dixon et al. 2007).

We will address these and other issues in this paper by analyzing the orbital evolution of a mass-gaining planet embedded in a gas disk. In section 2 we analyze the torque distributions for planets of constant mass on fixed circular orbits. In section 3 we analyze the orbital and mass evolution of migrating planets that undergo runaway mass accretion. Section 4 describes a model that appears to exhibit migration that is dominated by coorbital torques, i.e., Type III migration. Section 5 contains the summary and discussion.

2. TORQUE DISTRIBUTION FOR A NON-MIGRATING PLANET

Disk-planet gravitational torques result in planet migration (Goldreich & Tremaine 1980; Lin & Papaloizou 1993; Ward 1997). The distribution of torque with disk radius provides a means of connecting the theory with simulations. In this section, we model the disk as a three-dimensional system and consider fixed mass planets on fixed circular orbits. The torque per unit radius for a planet embedded in a disk was previously considered in Bate et al. (2003). Here we reconsider the analysis with higher resolution, especially in the coorbital region, and apply the torque distribution per unit disk mass.

2.1. Numerical Procedure

In this section, we describe the torques exerted by a disk on an embedded planet with mass, M_p , equal to $1 M_E$, $10 M_E$, $0.3 M_J$, and $1 M_J$. For the two smallest mass planets we consider, the planet's Hill radius is smaller than the vertical disk thickness of several percent of the distance to the star. For the two largest mass planets, the Hill radius is comparable or larger than the disk thickness.

2.1.1. Disk Model

We use spherical polar coordinates $\{R, \theta, \phi\}$, with the origin located at the star-planet center of mass. The reference frame corotates with the star-planet system. The planet's orbit lies in the plane $\theta = \pi/2$. The disk is assumed to be symmetric with respect to this plane, hence only the disk's northern hemisphere (i.e., the volume $\theta \leq \pi/2$) is simulated.

We assume that the material in the disk is locally isothermal and that the pressure p is given by

$$p(R, \theta, \phi) = \rho(R, \theta, \phi) c_s^2(r), \quad (1)$$

where $\rho(R, \theta, \phi)$ is the mass density. Quantity $c_s(r)$ is the gas sound speed, which is taken to be a function of cylindrical radius $r = R \sin \theta$. The aspect ratio of the disk,

H/r , is taken to be constant and equal to 0.05. Therefore, the temperature distribution in the disk is only a function of the distance from the disk's rotation axis, r , and decreases as $c_s^2 \propto 1/r$. Viscous forces are calculated by adopting the stress tensor for a Newtonian fluid (Mihalas & Weibel Mihalas 1999) with constant kinematic viscosity, ν and zero bulk viscosity. Disk self-gravity is ignored. In Appendix C, we discuss some effects of disk self-gravity and of the axisymmetric component of disk gravity on the migration rates.

2.1.2. Disk and Planet Parameters

We adopt the stellar mass M_s as unit of mass, the orbital radius a as unit of length, and $\Omega_p^{-1} = [G(M_s + M_p)/a^3]^{-1/2}$ as unit of time. In converting to dimensional units we consider $a = 5.2 \text{ AU}$ and $M_s = 1 M_\odot$.

The disk extends from 0 to 2π in azimuth around the star and, in radius, from 0.4 to either 4.0 (Jupiter-mass case) or 2.5 (lower mass cases). In the θ -direction, the disk domain extends above the midplane ($\theta = \pi/2$) for 10 degrees, comprising 3.5 pressure scale heights, H . The initial mass density distribution is independent of ϕ , has a Gaussian profile in the θ -direction, and has a radial profile proportional to $R^{-3/2}$, so that the initial (unperturbed) surface density varies as $R^{-1/2}$. We adopt a constant dimensionless kinematic viscosity ν equal to 10^{-5} , corresponding to a turbulent viscosity parameter $\alpha = 0.004$ at the cylindrical radius $r = 1$ (5.2 AU).

As mentioned above, we perform calculations for four planet masses: $M_p = 3 \times 10^{-6}$, 3×10^{-5} , 3×10^{-4} , and 1×10^{-3} , which correspond, respectively, to $1 M_E$, $10 M_E$, $0.3 M_J$, and $1 M_J$. The gravitational potential, Φ_p , of the planet is smoothed over a length ϵ equal to $0.1 R_H$ and is given by

$$\Phi_p = -\frac{GM_p}{\sqrt{S^2 + \epsilon^2}}, \quad (2)$$

where S is the distance from the planet and R_H is the Hill radius of the planet.

2.1.3. Numerical Method

The mass and momentum equations that describe the evolution of the disk (e.g., DBL05) are solved numerically by means of a finite-difference scheme that applies an operator splitting procedure to perform the spatial integration of advection and source terms (Ziegler & Yorke 1997). The algorithm is second-order accurate in space and semi-second-order accurate in time. The equations are discretized over a mesh with constant grid spacing in each coordinate direction. Nested grids are used to enhance the numerical resolution in (arbitrarily large) regions around the planet (D'Angelo et al. 2002, 2003). This strategy allows the volume resolution to be increased by a factor 2^3 for each added grid level. These calculations are executed with grid systems involving 5 levels of grid nesting. The linear base resolution is $\Delta R = a \Delta \theta = a \Delta \phi = 0.014 a$. The linear resolution achieved in the coorbital region around the planet is approximately $9 \times 10^{-4} a$, which corresponds to $\sim 0.01 R_H$ and $\sim 0.1 R_H$ in the Jupiter-mass and Earth-mass cases, respectively. To quantify resolution effects in the Earth-mass case, we also applied a linear resolution twice as

high throughout the entire grid system (base resolution of $7 \times 10^{-3} a$ and resolution in the coorbital region around the planet of $4 \times 10^{-4} a$). The torques at the two resolutions, integrated over the disk domain, differ by about 5%.

The boundary condition near the planet involves removing gas from $\sim 0.1 R_H$ of the planet at each timestep. The procedure for mass removal is described in more detail in section 3.1.1. In the calculations reported in section 2.3, the removed mass is not added to the planet's mass in order to keep it fixed. In sections 3 and 4 (as well as in Appendix A and C), we will present cases in which the planet's mass is augmented by the mass of the gas removed from the disk.

The outer boundary of the disk domain is closed to both inflow and outflow, whereas the inner boundary allows outflow (material can flow out of the grid domain) but not inflow. Reflective and symmetry boundary conditions are applied at colatitude $\theta = \theta_{\min}$ and at the disk mid-plane ($\theta = \pi/2$), respectively.

Simulations are run for about 100 orbital periods. In models with $0.3 M_J$ and $1 M_J$ mass planets, the initial density distribution includes a gap along the planet's orbit to account for an approximate balance between viscous and tidal torques, which reduces the relaxation time towards steady state. In all calculations discussed here, the flow achieves a fairly steady state within ~ 100 orbits.

2.2. Theoretical Considerations

2.2.1. Torque Density

Consider a cylindrical coordinate system $\{r, \phi, z\}$ centered on the star-planet center of mass. The disk torque along the rotation axis per unit radius exerted on the planet is given by

$$\frac{dT}{dr}(r, t) = \left\langle r \int_0^{2\pi} d\phi \int_{-\infty}^{\infty} dz \rho(\mathbf{r}, t) \partial_\phi \Phi_p(\mathbf{r}, t) \right\rangle, \quad (3)$$

where $\langle X(t) \rangle$ denotes the time-average of X over an orbit period centered about time t , ρ is the gas density, and Φ_p is the potential due to the planet (eq. 2).

2.2.2. Radial Overlap Regions

The linear theory of Lindblad resonances for disk-planet interactions demonstrates that the strongest contributing resonances have azimuthal wavenumbers $m \sim r/H$. This estimate comes from considering the so-called torque cutoff effect that arises from Lindblad resonances that lie close to the planet (Goldreich & Tremaine 1980; Ward 1986; Artymowicz 1993). As a consequence of the resonance condition, we expect the peak torque density to be at a distance of roughly H from the planet. The torque cutoff is not sharp and there are torque contributions from resonances that lie closer than distance $\sim H$ from the planet, although at a decreasing level as they get closer to the planet. As we will see, the numerical results show the torque density peak to be close to distance H from the planet. However, the torque cutoff calculations assume that the orbits are such that the gas azimuthally passes by the planet, i.e. lies on circulating orbits. On the other hand, close to the planet's orbit, this assumption breaks down and the gas flows on librating streamlines of the horseshoe orbit region. This region

generally extends in the radial direction to a distance of about $3 R_H$ from the planet's orbital radius, where R_H is the planet's Hill radius. But, close to the planet, the region becomes less extended radially, spanning only to approximately R_H . That is, the noncoorbital (circulating) streamlines pass closest to the planet at a distance about equal to R_H (see streamline a in Lubow et al. 1999 and Figure 5 in Bate et al. 2003). In the horseshoe orbit region, the corotational resonance can play a role.

These two regions, the coorbital region (extending up to about $3 R_H$ from the planet's orbital radius) and Lindblad torque region (extending beyond about distance H from the planet's orbital radius), overlap in a one-dimensional radial sense for planet-to-star mass ratios

$$q \gtrsim \frac{1}{9} \left(\frac{H}{r} \right)^3. \quad (4)$$

This condition does not necessarily imply a physical overlap in two or three dimensions. But it does affect our interpretation of the torque density reduced to one dimension, $dT(r)/dr$. The reason is that for a given radius r such that $R_H < |r - a| < 3 R_H$, the gas lies in either the coorbital (librating) or noncoorbital (circulating) region, depending on the azimuth.

For the disk parameters considered in this section, the one-dimensional overlap occurs for planet masses greater than about $4.6 M_E$, which covers all, but one, of the planet masses considered. For a $1 M_J$ planet, this overlap occurs out to a radius of about $1.2 a$ or a radial distance of about $4 H$ from planet.

The two regions physically overlap in a two- or three-dimensional sense, when the closest approach of all noncoorbital (circulating) streamlines, which occurs at a distance $\sim R_H$ from the planet, is greater than the distance where there are maximum Lindblad torques ($\sim H$). This occurs when

$$q \gtrsim 3 \left(\frac{H}{r} \right)^3. \quad (5)$$

In this case, the usual torque cutoff condition for Lindblad resonances is questionable. This argument suggests that the torque density maximum for Lindblad resonances should occur at a radial distance from the planet

$$|r - a| \simeq \max(R_H, H). \quad (6)$$

When this condition is satisfied, the overall torque on the planet will be reduced, even if $R_H \lesssim H$, since resonances that lie closer than distance H from the planet are suppressed³. For the disk parameters considered in this section, this condition is satisfied for $M_p \gtrsim 4 \times 10^{-4} M_s$ (or $0.4 M_J$).

2.2.3. Saturation Effects of Coorbital Torques

The flow in the coorbital region is trapped in horseshoe orbits. For a time-reversible system (e.g., no dissipation or migration), the streamlines are exactly periodic and no net torque occurs on the planet due to the disk (i.e., the torque saturates), except for possible initial transients due to initial conditions. However, turbulent viscosity introduces irreversibility that can lead to a net torque. The condition for saturation within the framework of the

³ They may still partially contribute, due to their finite widths.

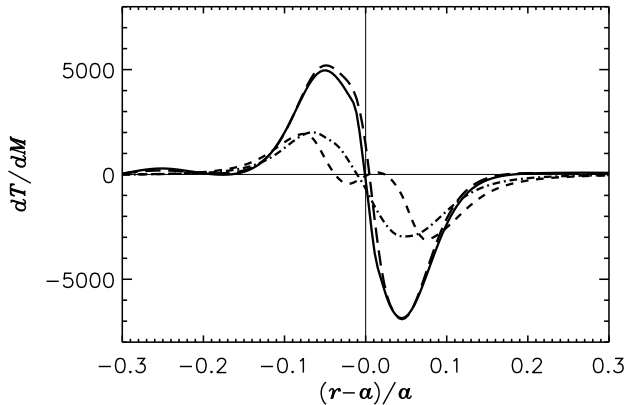


FIG. 1.— Torque per unit disk mass on the planet as a function of radius in units of the planet’s semi-major axis, a . The vertical scale is in units of $GM_s(M_p/M_s)^2/a$. The solid, long-dashed, dot-dashed, and short-dashed curves are for $1 M_E$, $10 M_E$, $0.3 M_J$, and $1 M_J$ mass planets, respectively. The disk is modeled as a three-dimensional system. The vertical disk thickness is $H/r = 0.05$ for all the cases. Torque distributions are averaged over one orbital period.

α -disk model is that the libration timescale of the fluid in the coorbital region is shorter than the viscous radial diffusion timescale across this region. Based on scaling arguments, the saturation condition is given by (Ward 1992)

$$\alpha \lesssim q^{3/2} \left(\frac{r}{H} \right)^{7/2}. \quad (7)$$

For the parameters in this section, this constraint implies that for planets of order $10 M_E$ or greater, the corotation torques should be saturated (small). Saturation effects should be important for the larger planet masses we consider.

2.3. Numerical Results

The torque per unit disk mass is defined by

$$\frac{dT}{dM}(r, t) = \left\langle \frac{1}{2\pi\Sigma(r, t)} \int_0^{2\pi} d\phi \int_{-\infty}^{\infty} dz \rho(\mathbf{r}, t) \partial_\phi \Phi_p(\mathbf{r}, t) \right\rangle, \quad (8)$$

where $\Sigma(r, t)$ is the axisymmetric disk density (i.e., the surface density averaged over the azimuth ϕ) and notation $\langle X(t) \rangle$ is defined below equation (3).

Numerically, the torque distribution per unit disk mass is determined by dividing the (three-dimensional) disk into a series of concentric shells, of radius R and thickness ΔR , centered at the origin and calculating the torque exerted by the shell and the mass of the shell. The torque per unit disk mass is obtained from the ratio of these two quantities⁴, averaged over an orbit period. We use the radial grid spacing on the base grid for the value of ΔR . The torques arising from within the Hill sphere of the planet are ignored in this section, but are included in later sections of this paper. We ignore such considerations here in order to compare results with the standard theory of coorbital and Lindblad torques, which does not include such contributions (Tanaka et al. 2002).

⁴ There is a slight error of order $(H/r)^2$ in this procedure due to the difference between the spherical coordinate system used in the calculations and the cylindrical coordinates that apply to the definition of the torque in equation (3).

The torque per unit disk mass for four planet mass cases is shown in Figure 1. The plots are normalized such that the torque densities in the four cases would be the same, according to linear theory, if the axisymmetric disk density gradients and gas properties (sound speeds and viscosities) were the same. That is, the torque density per unit disk mass is scaled by the square of the star-to-planet mass ratio. The $1 M_E$ (solid line) and $10 M_E$ (long-dashed line) cases nearly exactly overlap as predicted, while the $0.3 M_J$ (dot-dashed line) and $1 M_J$ (short-dashed line) cases have a smaller scaled torque density. The scaling in the plot masks the fact that the results span a large range of parameter space. In going from $1 M_E$ to $1 M_J$ there is a change in torque density by a large factor, 10^5 , while the discrepancy is about a factor of 2.5.

The deviations in the $0.3 M_J$ and $1 M_J$ cases could be due to the modified torque cutoff, pressure gradients, and nonlinearities. Since $R_H \gtrsim H$ in these cases, Lindblad resonance contributions are weakened by the modified torque cutoff, as discussed in Section 2.2.2. Pressure gradients cause shifts in the resonance locations. For mild pressure gradients that change sign across the orbit of the planet (as would occur for a mild gap), the resonances shift away from the orbit of the planet (see eq. 26 of Ward 1986). The shift would then cause the torques per unit disk mass to be weaker, as seen in the figure. The situation is more complicated in the case of stronger pressure gradients, as may occur for deep gaps, and the sign of the effect on the torque depends on the detailed shape of the density profile. Nonlinearities may play a role in the $1 M_J$ case, since there are shocks in the disk in that case, due to the strong forcing. But the total torque is not expected to be substantially affected by nonlinearity. For a fixed smooth background disk density distribution, resonant torques are quite insensitive to the level of nonlinearity (Yuan & Cassen 1994). For a $1 M_J$ planet and a resonance with azimuthal wavenumber $m = 20 = H/a$, the nonlinearity is mild with nonlinearity parameter $f = 0.6$, as defined by Yuan & Cassen (1994). Some broadening of the torque density profile is predicted, while the total torque is reduced by only about 1%. For much stronger nonlinearity, $f = 3$, the torque reduction is only 5%. This estimate is based on considering only a single resonance. Many resonances overlap, increasing the level of nonlinearity. However, the theory does not describe overlapping resonances. So, although we cannot be definite about the importance of nonlinearities, indications for a single resonance suggest that they are not important.

The torque density per unit disk mass for the $1 M_J$ planet in Figure 1 (short-dashed line) shows indications of saturation for $|r - a| < R_H$. As discussed above, this effect is suggested by theoretical considerations. The torque density peak for the $1 M_J$ case is slightly displaced away from the planet relative to the smaller mass cases and lies close to a distance $R_H \simeq 0.07 a$ from the planet. This result is consistent with equation (6) in the $1 M_J$ case, $|r - a| \simeq 0.07 a = 1.4 H$.

Figure 2 shows that the torque in the $1 M_J$ case is acquired close to the planet, well within the gap region. Most of the torque is accumulated by material with intermediate/low density interacting with an intermediate magnitude torque per unit disk mass. About 80% of the

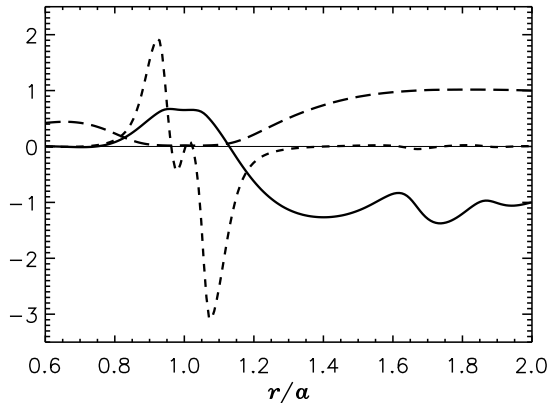


FIG. 2.— Azimuthally averaged surface density (*long-dashed curve*), disk torque per unit disk radius exerted on the planet (*short-dashed curve*), and cumulative torque (*solid curve*), i.e., torque per unit radius integrated outward, as a function of radius for a $1 M_J$ planet on a fixed circular orbit. The disk is modeled as a three-dimensional system. The unit of radius is the planet’s orbital radius a . The surface density and cumulative torque are normalized by their absolute values at $r = 2$. The disk torque per unit disk mass is normalized by $10^3 GM_s (M_p/M_s)^2/a$. The plotted values are averaged over one orbital period.

torque is due to material within a radial distance of $0.25 a$ from the planet.

3. MIGRATING AND GROWING PLANETS

We investigate the orbital migration of a planet that is undergoing run-away gas accretion. We consider several disk configurations, by changing the initial surface density, the pressure scale height, and the kinematic viscosity. We use disk models and numerical procedures similar to those introduced in section 2.1. Throughout this section, the disk is modeled as a three-dimensional system. The origin of the coordinate system is taken to be the star. The coordinate system rotates about the origin at a rate equal to the rotation rate of the planet around the star. We integrate the equations of motion of the planet, under the action of disk torques and apparent forces arising from the rotation of the reference frame, as described in DBL05. The unit of length is the initial star-planet separation a_0 (or 5.2 AU when converting into physical units). The unit of time is the inverse of Ω_0 , the initial angular speed of the planet. The unit of mass is the stellar mass M_s ($1 M_\odot$).

The grid system achieves a linear base resolution of $\Delta R = a_0 \Delta \theta = a_0 \Delta \phi = 0.014 a_0$. In the coorbital region around the planet, the linear resolution is about $9 \times 10^{-4} a_0$. Nested grid levels cover extended radial regions of the disk so that the planet remains within the domain covered by the most refined grid level over the entire orbital evolution. Convergence tests were carried out with a grid system that used a volume resolution $(3/2)^3$ times as high throughout the whole disk domain and on all grid levels. No significant differences are observed (see Appendix A.1). To avoid depletion of the disk interior of the planet’s orbit, we apply nonreflecting boundary conditions to the inner grid (radial) border. We test our results against possible boundary condition effects in Appendix A.2 by applying outflow boundary conditions and moving radial disk boundaries farther away from the

planet’s orbit in both directions. No important effects are observed. Near the planet we apply accreting boundary conditions on the gas, as described in section 3.1.1. We consider planetary mass increases that extend over more than two orders of magnitude and a range of disk surface densities.

To avoid possible spurious torques exerted by material gravitationally bound to the planet, contributions from within $R_H/2$ of the planet are not taken into account. We report in Appendix A.3 on the sensitivity of the results to the radius of the excluded region by considering a smaller radius. We find that the changes are not significant.

We generally initiate the calculations with a planet mass $M_p = 1.5 \times 10^{-5} M_s$, or $5 M_E$. However, in some applications discussed in section 4, we use an initial mass $M_p = 3 \times 10^{-4} M_s$ (about $0.3 M_J$) in order to study the effects on migration of releasing a more massive planet in an unperturbed disk.

3.1. Planet Mass Growth

3.1.1. Gas Accretion

In the core accretion scenario of giant planet formation, prior to the phase of run-away gas accretion, the rate at which gas is accreted is largely determined by the ability of a planetary core’s envelope to radiate away the energy delivered by gas and solids (phase of slow gas accretion, see e.g., Hubickyj et al. 2005). During the initial stages of planet growth, the accretion of solids dominates, and the dissipation of the kinetic energy of the impacting solids provides an important heat source for the accreted gaseous envelope. Models of Hubickyj et al. (2005), which ignore the effects of planet migration, experience a depletion of solid disk material in the vicinity of the planet and consequently a reduction in the envelope heating rate. When the mass of the gas (in the envelope) is comparable to the mass of solids (in the core), the pressure gradient cannot prevent the gravitational collapse of the envelope. This situation results in a sudden increase of the gas accretion rate and a rapid growth of the planet’s mass, the so-called run-away gas accretion phase (e.g., Wuchterl 1993; Pollack et al. 1996).

The models presented here assume run-away gas accretion. They do not account for the thermal structure and detailed microphysics of a planet’s envelope. Therefore, we do not determine self-consistent gas accretion rates, prior to the phase of run-away gas accretion ($M_p \lesssim 10 M_E$). The models also ignore the effects of heating by impacting solids that act to slow the gas accretion, as the planet migrates out of the region of depleted solids. During the run-away gas accretion phase, the accretion rate onto the planet is only limited by the amount of gas that the disk is able to supply. The calculations described here provide estimates of such limiting gas accretion rates during the run-away gas accretion phase.

In these models, we adopt a prescription that gas within a distance of $R_{\text{acc}} = 0.1 R_H$ from the planet can accrete onto it. Accreted gas is removed from the disk and its mass is added to the planet mass. For the models we consider, this distance is safely smaller than the possible characteristic accretion radii: the Hill radius, R_H , and the Bondi radius, R_B (distance beyond which the thermal energy of the gas is larger than the gravi-

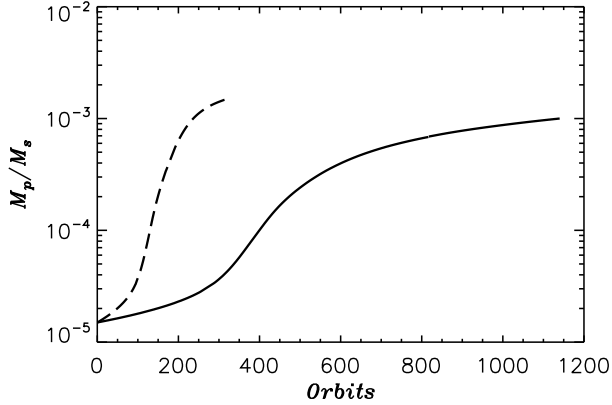


FIG. 3.— Mass evolution of a protoplanet having initial planet mass $5 M_E$ undergoing run-away gas accretion in a three-dimensional disk with initial surface density $\Sigma_p = 3 \times 10^{-4} M_s a_0^{-2}$ or about 100 g cm^{-2} at the planet's initial orbital radius of 5.2 AU (solid line) and $\Sigma_p = 9 \times 10^{-4} M_s a_0^{-2}$ or about 300 g cm^{-2} (dashed line). In both cases, the disk thickness is $H/r = 0.05$ and the turbulent viscosity parameter is $\nu = 1 \times 10^{-5} a_0^2 \Omega_0$ ($\alpha = 0.004$ at 5.2 AU). The time refers to orbits at $a_0 = 5.2 \text{ AU}$ or about 12 years.

tational energy that binds the gas to the planet). The distance R_{acc} is at least a factor of 3 smaller than R_B . Therefore, this mass removal prescription should not determine the accretion rate for the case of run-away gas accretion (see also Tanigawa & Watanabe 2002). The amount of material accreted per time-step Δt is given by $(\Delta t/\tau_{\text{acc}}) \int \rho dV$, where dV is the volume element and τ_{acc} is a removal timescale. The integral is performed over the sphere of radius $0.1 R_H$ centered on the planet. Here we set $\tau_{\text{acc}} = 0.1 \Omega_0^{-1}$ within the sphere of radius $0.05 R_H$ and $\tau_{\text{acc}} = 0.3 \Omega_0^{-1}$ for $0.05 R_H < S < 0.1 R_H$ (S is the distance from the planet).

3.1.2. Mass Evolution

In this section we describe the accretion rates of migrating, mass-gaining planets. Figure 3 shows the planet mass as a function of time, $M_p = M_p(t)$, for a model with initial (unperturbed) surface density at the initial orbital radius of the planet $\Sigma_p = 3 \times 10^{-4} M_s a_0^{-2}$ (solid line). For a planet orbiting a Solar mass star at 5.2 AU, this density is about 100 g cm^{-2} , roughly corresponding to the minimum mass solar nebula.

The mass evolution can be understood in terms of Bondi and Hill accretion. Consider a simple model in which gas is captured within some radius, S_c , of a planet and assume $S_c < H$. Mass is accreted with some velocity relative to the planet of order ΩS_c , and so the mass accretion rate in a three-dimensional disk (where $\rho \approx \Sigma/H$) is estimated as

$$\dot{M}_p \sim \frac{\Sigma}{H} \Omega S_c^3, \quad (9)$$

where we take S_c as either the Bondi or Hill radius, with the Bondi radius given by $R_B = G M_p/c_s^2$ and the Hill radius given by $R_H = a [M_p/(3 M_s)]^{1/3}$.

In the case that gas pressure prevents the gas from being bound to the planet within the Hill sphere (or, equivalently, that pressure forces dominate over gravitational three-body forces), we expect the Bondi description to

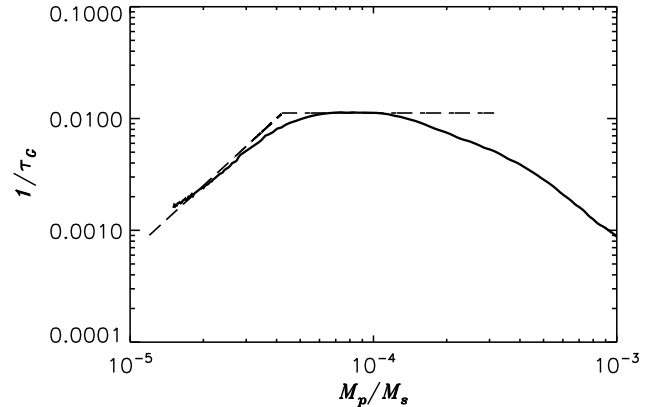


FIG. 4.— Mass growth rate $1/\tau_G = \dot{M}_p/M_p$ in units of inverse orbital periods at the initial radius of the planet, $\Omega_0/(2\pi)$, plotted against M_p/M_s for the solid curve case in Figure 3. The dashed line plots the growth rate according to equation (15). The slopes of the two dashed line segments are predicted by the model. The two free parameters, C_B and C_H , are dimensionless constants of order unity that control the intercepts and are fit to the solid curve. The slanted portion of dashed line corresponds to accretion within the Bondi radius, given by $1/\tau_B$ in equation (15) with $C_B = 2.6$. The horizontal portion of the dashed line corresponds to accretion within the Hill radius for a disk with no gap, given by $1/\tau_H$ in equation (15) with $C_H = 0.89$. At higher planet masses, the growth rates drop due to the presence of the tidally produced gap.

be appropriate. This condition is that

$$c_s^2 \gtrsim \frac{G M_p}{R_H} \quad (10)$$

or

$$R_B \lesssim R_H. \quad (11)$$

Therefore in the general case we take

$$S_c = \min(R_B, R_H). \quad (12)$$

It then follows that the Bondi and Hill mass growth rates, \dot{M}_p/M_p , of the planet are given by

$$1/\tau_B = C_B \Omega \frac{\Sigma a^2}{M_s} \left(\frac{a}{H}\right)^7 \left(\frac{M_p}{M_s}\right)^2, \quad (13)$$

$$1/\tau_H = \frac{1}{3} C_H \Omega \frac{\Sigma a^2}{M_s} \left(\frac{a}{H}\right), \quad (14)$$

where C_B and C_H are dimensionless coefficients of order unity. The overall mass growth rate is given by

$$1/\tau_G = \begin{cases} 1/\tau_B & \text{for } M_p < M_t \\ 1/\tau_H & \text{for } M_p \geq M_t \end{cases} \quad (15)$$

where

$$M_t = \frac{M_s}{\sqrt{3}} \sqrt{\frac{C_H}{C_B}} \left(\frac{H}{a}\right)^3 \quad (16)$$

is the transition planet mass where $\tau_H = \tau_B$.

In Figure 4, we plot the mass growth rate, $1/\tau_G$, for the solid curve case in Figure 3. We applied equation (15) and adopted constant values of $\Sigma = \Sigma(a_0)$, at time $t = 0$, and $\Omega = \Omega_0$. The figure shows that the Bondi and Hill accretion rates in equation (15) agree with the simulation results for values of $C_B = 2.6$ and $C_H = 0.89$. The transition mass in this case evaluates to $M_t = 4.2 \times 10^{-5} M_s$. It lies between the Bondi and

Hill accretion regimes in the figure, at the intersection between the two dashed line segments. For larger values of planet mass, $M_p \gtrsim 2 \times 10^{-4} M_s \approx 4.8 M_t$, this simple estimate of the mass growth rate breaks down because the density is depleted near the planet due to the onset of gap formation. The density near the planet is reduced by about 40% when $M_p \approx 2 \times 10^{-4} M_s$ (see Fig. 6, *right panel*). In addition, the Hill radius becomes comparable to H , since $R_H = H = 0.05 a$ for $M_p = 3.75 \times 10^{-4} M_s$.

Simulations carried out in two dimensions would have different scaling behavior, since the right-hand side of equation (9) would be $\Sigma \Omega S_c^2$. The dependence of the mass accretion rate on planet mass and disk sound speed then artificially deviates from the three-dimensional case. In two dimensions we have that $1/\tau_B \propto (M_p/M_s) (a/H)^4$ and $1/\tau_H \propto (M_s/M_p)^{1/3}$.

The maximum of the accretion rate for the solid curve case of Figure 3 is $\dot{M}_p \sim 5 \times 10^{-3} \Sigma_p a^2 \simeq 1.5 \times 10^{-3} M_J$ per orbit and occurs when $M_p \approx 0.3 M_J$. This result is consistent with the previous findings of D’Angelo et al. (2003) and Bate et al. (2003), who considered planets on fixed orbits. Also displayed in Figure 3 is the planet’s mass evolution in a disk with initial $\Sigma_p = 9 \times 10^{-4} M_s a_0^{-2}$ (*dashed line*) or about 300 g cm^{-2} at 5.2 AU. For $M_p/M_s \lesssim 10^{-4}$, the accretion rate is a factor of 3 larger than that of the lower density disk case (*solid line*). Hence, equation (15) applies to the growth rate with the same coefficients C_B and C_H as those given above. For larger planet masses, the accretion rate keeps increasing until $M_p \approx 0.7 M_J$, at which point \dot{M}_p starts to decline very rapidly as M_p grows further. This is because effects due to gap formation are delayed. The timescale required to form a gap of half-width ξR_H is $\tau_{\text{gap}} \sim \xi^5 q^{-1/3} \Omega^{-1}$ (see, e.g., Bryden et al. 1999), where $\xi \approx 2$ (see *long-dashed line* in Fig. 2). In the lower density disk model (*solid curve* in Fig. 3), $\tau_{\text{gap}} < \tau_G$ for $M_p/M_s \gtrsim 10^{-4}$. In the higher density disk model (*dashed curve*), τ_{gap} becomes shorter than τ_G only when $M_p \gtrsim 0.7 M_J$.

In Figure 5, the mass evolution is shown for cases in which $\Sigma_p = 3 \times 10^{-4} M_s a_0^{-2} \approx 100 \text{ g cm}^{-2}$, but with different scale heights, H , and kinematic viscosities, ν . Near $M_p = 1 M_J$, the accretion rates of the two models with different H/r (*solid and long-dashed lines*), but the same Σ_p and ν , are nearly equal, with $\dot{M}_p \approx 3 \times 10^{-3} \Sigma_p a^2 \simeq 9 \times 10^{-4} M_J$ per orbit. At larger planet masses, \dot{M}_p is smaller in the case of a colder disk (*long-dashed line*) because of the stronger tidal torques exerted by the planet on the disk material that produce a wider gap. When $M_p \approx 1 M_J$, the simulation with 10 times larger viscosity (*short-dashed line*) yields an accretion rate that is a factor of nearly 8 larger. This result is consistent with previous two-dimensional studies of planets on fixed orbits that do not gain mass. For $M_p \approx 1 M_J$ these studies showed that \dot{M}_p scales approximately linearly with $\nu \Sigma$, the overall disk accretion rate evaluated just outside the gap (Kley 1999; Lubow & D’Angelo 2006).

3.1.3. Mass Within the Hill Sphere

We discuss here the relevance of torques exerted on a planet and originating within the planet’s Hill sphere.

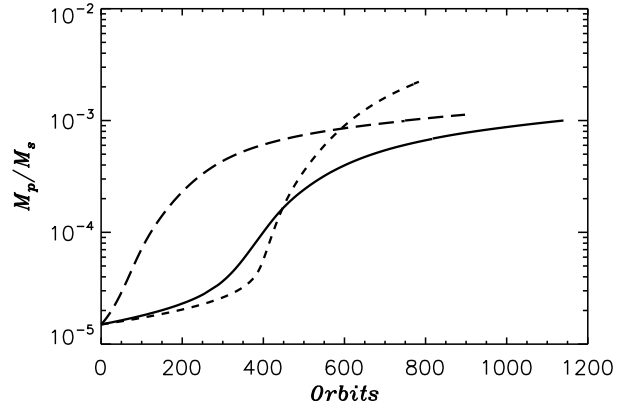


FIG. 5.— Mass evolution of a protoplanet having initial planet mass $5 M_E$ and undergoing run-away gas accretion in a three-dimensional disk with initial surface density $\Sigma_p = 3 \times 10^{-4} M_s a_0^{-2} \approx 100 \text{ g cm}^{-2}$ at the planet’s initial orbital radius $a_0 = 5.2 \text{ AU}$. The solid line represents a case with $H/r = 0.05$ and turbulent viscosity $\nu = 1 \times 10^{-5} a_0^2 \Omega_0$ ($\alpha = 0.004$ at 5.2 AU), the long-dashed line refers to a variant model with $H/r = 0.04$ and the same ν value ($\alpha = 0.006$ at 5.2 AU), and the short-dashed line represents a variant model with $\nu = 1 \times 10^{-4} a_0^2 \Omega_0$ ($\alpha = 0.04$ at 5.2 AU). The time refers to orbits at $a_0 = 5.2 \text{ AU}$ or about 12 years.

We may expect that material gravitationally bound to the planet should not be capable of exerting significantly strong torques, if resolution is appropriate (DBL05). In some situations, if the local density is large, any torque imbalance can be easily amplified by lack of numerical resolution (because torques depend on $1/S^2$, where S is the distance to the planet). Artificial effects may arise when the mass within $\sim R_H$ of the planet is larger than the planet’s mass. However, not all this material is necessarily bound to the planet. Because of the nonspherical nature of the Roche lobe, the Hill radius represents an overestimate for the size of the region where gas is bound to the planet (Paczynski 1971; Eggleton 1983). We have found that accumulated gas may be bound to the planet within distances shorter than $R_H/2$ from the planet (see Appendix D.1).

In all the cases discussed in this section, the amount of material that lies within $R_H/2$ of the planet is smaller than M_p , throughout the evolution, by several orders of magnitude. For models in Figure 3, as well as for those in Figure 5, the ratio of these two masses ranges from less than $\sim 10^{-3}$ to $\sim 10^{-2}$, depending mainly on the planet’s mass. We also consider models with initial densities larger than those discussed here (described in section 4). However, this mass ratio remains on the order of 10^{-2} or smaller. Therefore, due to the accretion boundary condition employed here at the planet location, these models do not experience a build-up of mass near the planet (with possible effects on planet migration). The accreted mass is accounted for by the increase in the planet mass.

3.2. Planet Migration

3.2.1. Theoretical Regimes of Migration

A planet that grows in mass from a few Earth-masses to a few Jupiter-masses is susceptible to two “classical” regimes of migration. The Type I regime is expected

when the planet causes small, linear disk density perturbations (e.g., [Ward 1997](#); [Tanaka et al. 2002](#)). In the opposite limit, Type II occurs when the planet mass is large enough to cause nonlinear density perturbations that result in a density gap along its orbit ([Lin & Papaloizou 1986](#)).

For the parameters we adopt (pressure scale height $H/r \sim 0.05$, kinematic viscosity of disk $\nu \geq 1 \times 10^{-5} a_0^2 \Omega_0$, and initial planet mass $M_p/M_s = 1.5 \times 10^{-5}$ (or $M_p = 5 M_E$), it is expected that the initial evolution of the planet will follow Type I migration, since the usual gap opening criteria are not satisfied. In the linear theory of [Tanaka et al. \(2002\)](#), the rate of migration resulting from the action of both Lindblad and (unsaturated) coorbital corotation torques is given by

$$\frac{da_I}{dt} = -(2.73 + 1.08 s) \left(\frac{M_p a}{M_s H} \right)^2 \frac{\Sigma_p}{M_p} a^3 \Omega_p, \quad (17)$$

where s is the slope of the unperturbed surface density. For the case of saturated (zero) coorbital corotation torques, the migration rate is given by

$$\frac{da_I}{dt} = -(4.68 - 0.20 s) \left(\frac{M_p a}{M_s H} \right)^2 \frac{\Sigma_p}{M_p} a^3 \Omega_p. \quad (18)$$

The conditions for saturation are discussed in section [2.2.3](#). For higher planet masses that arise in the later stages of the simulations, the torques are expected to be saturated.

In the presence of a sufficiently clean density gap and for a planet whose mass is less than the local disk mass, the rate of migration follows Type II theory that is dictated by disk viscous inflow

$$\frac{da_{II}}{dt} = -\zeta \frac{\nu}{a}. \quad (19)$$

Note that if there is residual material in the horseshoe orbit region, the migration rate can differ from that in equation (19). The coefficient ζ on the right-hand side of equation (19) is of order unity and also depends on the evolutionary state of the disk. For a steady-state disk, the coefficient is $3/2$. But for nonsteady disks where $\nu\Sigma$ varies in radius, as in our initial states, the coefficient may differ by order unity amounts.

In the unsaturated case, some nonlinear effects of the corotation resonance can cause migration rates to differ from those predicted by equation (17) ([Masset et al. 2006](#)). For $s = 1/2$, $H/r = 0.05$, these effects occur in the range of masses is between $\approx 10 M_E$ and $\approx 20 M_E$. However, in the models presented here, the planet grows too quickly through this mass range (taking less than a few tens of orbits) to significantly affect migration (see [Fig. 23](#) in [Appendix B](#)).

When the amount of material in the horseshoe orbit region is larger than the planet's mass, a regime of fast migration known as Type III may occur. The origins of such a regime are not yet entirely clear. The model of MP03 suggests that it is driven by strong corotation torques originating from material that streams past the planet, while the planet is moving in the radial direction. However, an analytic model of OL06 suggests that such torques could originate from trapped librating gas. A somewhat similar model was developed by [Artymowicz \(2004\)](#).

3.2.2. Orbital Radius Evolution

We evaluate quantities Σ_p , H , and Ω_p at the planet's orbital radius, a . Surface density $\Sigma_p = \Sigma_p(a)$ is evaluated according to its initial value $\Sigma_p(a) \propto (a_0/a)^s$, and so ignores evolutionary effects and tidal gap formation. The planet mass M_p is regarded as a function of time that we obtain from our simulations, via piecewise polynomial fits. For the numerical models we consider, $s = -d \ln \Sigma_p / d \ln a = 1/2$. Equations (17) and (18) are then solved numerically, providing the migration tracks $a_I = a_I(t)$.

In the left panel of [Figure 6](#), we compare such tracks with outcomes from our simulations. For the first 400 orbits, while $R_H \lesssim 0.9 H$ and $M_p \lesssim 0.27 M_J$, the orbital radius (i.e., semi-major axis) evolution is in good agreement with the results of Type I migration. The unsaturated coorbital torques appear to give a better fit than the saturated ones. But this is not always the case, as we see later when different disk parameters are considered. The right panel of [Figure 6](#) plots the density evolution of the gas near the planet, Σ_B , computed as ratio of the disk mass in the radial band $|r - a|/a \leq H/r$ to the area of the band (Σ_B^0 is the local initial value of Σ_B). It shows that the migration rate follows the Type I tracks on the left while the disk density near the planet remains close to the local initial disk value, assumed in equations (17) and (18). Up to a time of about 400 orbits, the density near the planet is reduced below its local initial value by less than 20%. At time of about 600 orbits, the density near the planet's orbit is reduced by about a factor of 3, and we should expect the migration rates deduced from the simulation to be substantially slowed below the rates based on Type I theory, in accord with the results on the left panel. After about 1000 orbits, when $M_p \gtrsim 0.9 M_J$, the migration rate in the simulation becomes comparable to the (local) viscous inflow rate (*long-dashed line*). At this point, the disk density near the planet is depleted by a factor of about 30.

The torque per unit disk mass as a function of distance from the planet for the case in [Figure 6](#) is plotted in [Figure 7](#). The plot shows very similar behavior to the case of a stationary, nongrowing planet seen in [Figure 1](#). Therefore, there is no evidence that planet migration or growth substantially affects the disk-planet torques for these model parameters. In particular, there is no evidence for strong coorbital torques.

The results obtained from a model with $H/r = 0.04$ (i.e., with a lower disk temperature compared to the model in [Fig. 6](#)) are shown in the left panel of [Figure 8](#). As in the case of the warmer disk, the Type I migration tracks (*short-dashed curves*) reproduce reasonably well the radial migration from the simulation (*solid line*) while $M_p \lesssim 0.14 M_J$ (see *long-dashed line* in [Fig. 5](#)) or $R_H \lesssim 0.9 H$. As before, the right panel of [Figure 8](#) shows that the migration rate follows the Type I tracks while the disk density near the planet remains close to the local unperturbed value. Again, when $M_p \gtrsim 0.75 M_J$, $\Sigma_B/\Sigma_B^0 \lesssim 0.03$ and $|da/dt|$ is on the order of the viscous inflow velocity (*long-dashed line*).

The dependence of migration on viscosity was investigated by running a simulation with kinematic viscosity $\nu = 1 \times 10^{-4} a_0^2 \Omega_0$ ($\alpha = 0.04$), ten times the value in [Figure 6](#) with all other parameters being the same. The

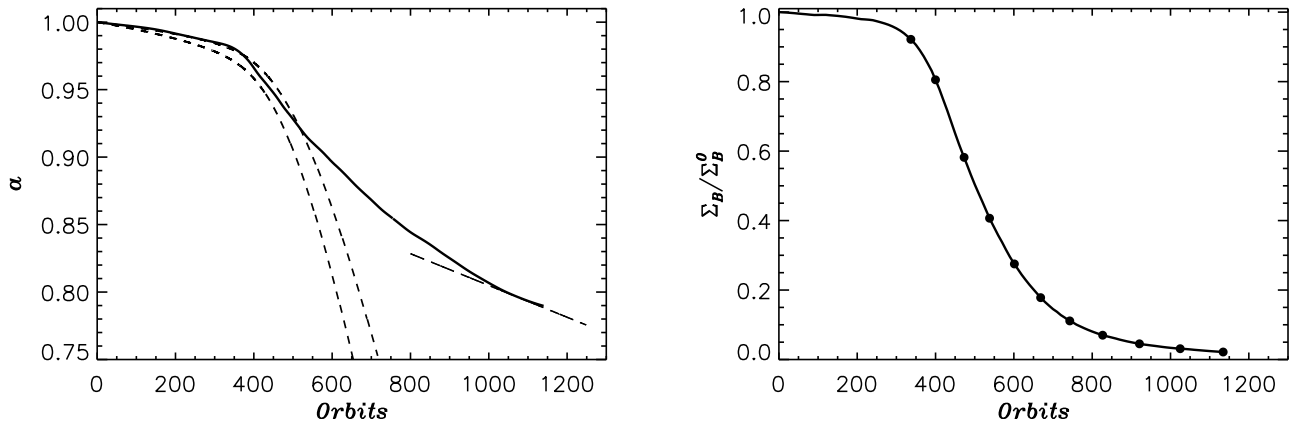


FIG. 6.— Orbital migration of a planet undergoing run-away gas accretion. *Left*: Orbital radius in units of a_0 (5.2 AU), as a function of time in units of the initial orbital period (≈ 12 years). The initial planet mass is $5 M_E$. The initial surface density is $\Sigma_p = 3 \times 10^{-4} M_s a_0^{-2} \approx 100 \text{ g cm}^{-2}$ at the planet’s initial orbital radius and $H/r = 0.05$. *Solid curve*: Results from the three-dimensional numerical simulation of a migrating, gas-accreting planet. *Short-dashed curves*: Predictions based on Type I migration theory, obtained by solving equations (17) and (18), for a planet that undergoes the mass growth given by the solid line in Figure 3 and is embedded in a disk with the initial unperturbed density distribution. The upper (lower) curve is for migration with unsaturated (saturated) coorbital torques. *Long-dashed line*: Consistent with Type II migration, the line has slope $-1.5\nu/a$ and passes through $a \approx 0.8a_0$ when $M_p \approx 0.9 M_J$. *Right*: Average disk density near the planet relative to the local initial value as a function of time. The density is averaged over a band of radial width $2H$ centered on the orbit of the planet (see text for details). Solid circles mark times when the mass ratio M_p/M_s is equal to 5×10^{-5} ($M_p = 16.7 M_E$) and when it is an integer multiple of 1×10^{-4} ($M_p = 33.3 M_E$).

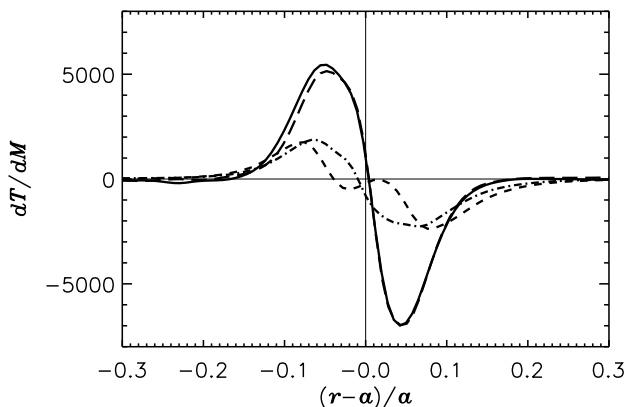


FIG. 7.— Torque per unit disk mass on the planet as a function of normalized distance from the migrating and growing planet plotted in Figure 6 ($\Sigma_p = 3 \times 10^{-4} M_s a_0^{-2} \approx 100 \text{ g cm}^{-2}$ at the planet’s initial orbital radius and $H/r = 0.05$). The vertical scale is in units of $GM_s(M_p/M_s)^2/a$, where $a = a(t)$. The solid, long-dashed, dot-dashed, and short-dashed curves refer to times when $M_p = 6.0 M_E$, $9.3 M_E$, $0.36 M_J$, and $1.0 M_J$, respectively.

results are shown in Figure 9. The left panel shows the orbital migration from the simulation as a solid curve and the Type I migration based on equations (17) and (18) as dashed curves. In this case, the relation $M_p = M_p(t)$ represented by a short-dashed line in Figure 5 is used in equations (17) and (18). The long-dashed line indicates a migration at a constant rate of $|\dot{a}| \approx 0.7\nu/a$, with $a \approx 0.9a_0$. The long-dashed line passes through a range of masses that spans from $\approx 0.2 M_J$ to $\approx 1.2 M_J$. However, at $M_p \approx 1 M_J$ ($t \approx 600$ orbits), the density gap along the planet’s orbit has not yet fully formed. This can be observed on the right panel of Figure 9, which displays the averaged disk density near the planet normalized to the local unperturbed (initial) disk value.

There is a drop of only a factor of 2.5 in the disk density near the planet by the time $M_p \approx 1 M_J$. The reason is that one of the conditions for steady-state gap formation, $M_p/M_s > 40\nu/(a^2\Omega) \sim 4 \times 10^{-3}$ (Lin & Papaloizou 1993), is not fulfilled in this higher viscosity case until $M_p \gtrsim 4 M_J$. At about 780 orbits, $\Sigma_B/\Sigma_B^0 \sim 0.1$ but the planet mass has reached beyond $2 M_J$ and is therefore more massive than the local disk mass. At those stages of the orbital evolution, inertia effects and further gap clearing are likely playing an important role in reducing the migration rate, as demonstrated in the next paragraph.

Figure 10 displays a comparison of the orbital radius evolution from two calculations. The solid line is the same as that in the left panel of Figure 9. The dotted line with solid circles is the outcome of a three-dimensional simulation in which the planet mass is fixed at $M_p = 1 M_J$. Material is removed from the vicinity of the planet according to the usual procedure we apply (see section 3.1.1), but in this case it is not added to the mass of the planet. The planet’s orbit is held fixed for the first 100 orbital periods, after which time it is allowed to evolve under the action of disk torques. The plot shows that there is general agreement, while $M_p \sim 1 M_J$, with the variable mass model and that the effect of adding mass to the planet in this regime is to slow its migration rate.

The local viscous timescale, $t_\nu = r^2/\nu$, in the models presented in Figures 9 and 10 is about 1600 orbital periods at $r = a_0$. Therefore, one might wonder whether the viscous evolution of the disk at radii larger than the outer grid boundary has any significant impact on the orbital evolution of the planet. We address this issue in Appendix B and show that extending the disk further out at larger radii does not affect the migration tracks shown in Figures 9 and 10. In Appendix B, we also present results for cases with viscosity parameter $\alpha = 0.2$ (kinematic

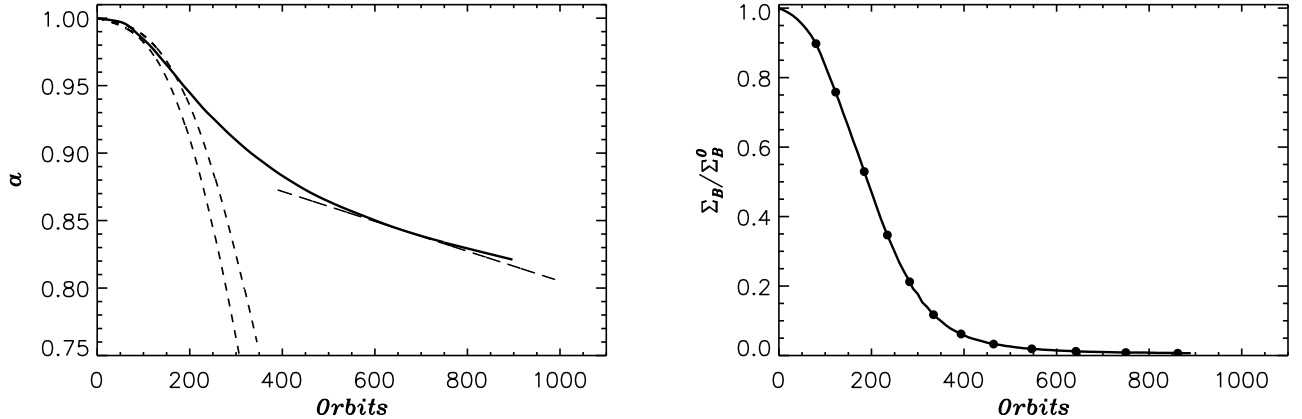


FIG. 8.— Orbital migration of a planet undergoing run-away gas accretion. Same as Figure 6, but for a cooler disk with aspect ratio $H/r = 0.04$ (the same ν and initial Σ_p). *Left*: The theoretical Type I migration tracks (*dashed curves*) use the mass evolution shown as a long-dashed curve in Figure 5. As in Figure 6, the upper (lower) short-dashed curve is for unsaturated (saturated) coorbital torques. The long-dashed line, representing Type II migration, has a slope equal to $-1.5\nu/a$ and passes through $a \approx 0.85a_0$, when $M_p \approx 0.9M_J$. *Right*: Normalized disk density near the planet as a function of time, as described on right panel of Figure 6 (see also text). Solid circles mark times when M_p/M_s is 5×10^{-5} ($M_p = 16.7M_E$) or an integer multiple of 1×10^{-4} ($M_p = 33.3M_E$).

viscosity $\nu = 5 \times 10^{-4} a_0^2 \Omega_0$) that have $t_\nu \simeq 320$ orbits at $r = a_0$. This case also leads to inward migration that can be interpreted as a Type I regime, partially modified by the perturbed surface density of the disk.

4. TYPE III MIGRATION

Figures 6 and 8 indicate that a growing planet undergoes Type I migration, as long the disk density near the planet remains undepleted. At higher planet masses where the gap opening sets in, there is a smooth transition towards Type II migration with migration speeds that are on the order of the viscous inflow velocity. There is no evidence for another form of migration, since the torque distributions are essentially the same in the migrating and nonmigrating cases explored thus far (compare Figures 1 and 7). Type III migration was suggested to involve coorbital material that provides a fast form of migration (MP03). In this section we discuss planet migration for several variants on the models of section 3 that should be favorable for a Type III regime of migration. We describe a case that appears to exhibit Type III migration.

4.1. Higher Disk Mass

Coorbital torques are stronger for higher mass disks. Masses in the coorbital region are on the order of $8\pi R_H a \Sigma(a)$. For the model presented in Figure 6, involving disks of relatively low density, the coorbital disk mass is approximately equal to the planet mass when $M_p \approx 0.2M_J$. We describe here results of three-dimensional calculations with initial surface densities $\Sigma_p = 9 \times 10^{-4} M_s a_0^{-2} \approx 300 \text{ g cm}^{-2}$ and $\Sigma_p = 1.5 \times 10^{-3} M_s a_0^{-2} \approx 500 \text{ g cm}^{-2}$ at the planet's initial orbital radius of $a_0 = 5.2 \text{ AU}$. The mass evolution in the former case is plotted as the dashed line in Figure 3. The mass evolution in latter case is similar, but the growth proceeds very rapidly reaching about $1M_J$ within 130 orbital periods. The resulting orbital radius evolution for both simulations is plotted in Figure 11 (*left panel*) along with the average disk density near the planet normalized to the local unperturbed value (*right panel*).

For both cases presented in the figure, at earlier times ($t \lesssim 170$ and $t \lesssim 100$ initial orbits, respectively), the simulated migration rates are comparable to the Type I rates. During that stage of the evolution, the coorbital region is more massive than the planet. In the model with initial $\Sigma_p \approx 300 \text{ g cm}^{-2}$ at 5.2 AU (upper migration track in Fig. 11), for times $t \lesssim 170$ orbits ($M_p \lesssim 0.3M_J$) the coorbital region mass to planet mass ratio is larger than 2. In the model with initial $\Sigma_p \approx 500 \text{ g cm}^{-2}$ at 5.2 AU (lower migration track Fig. 11), for times $t \lesssim 100$ orbits ($M_p \lesssim 0.4M_J$) the ratio of coorbital region mass to planet mass is larger than 3. However, during those stages, the results are generally consistent with the Type I migration and some slowing at later times, with no indication of another form of migration.

To examine the situation in more detail, we plot the torque per unit disk mass as a function of distance from the planet in Figure 12. The plot shows very similar behavior to the case of a nonmigrating, nongrowing planet seen in Figure 1, as well as to the case of a migrating, growing planet within a lower density disk presented in Figure 7. Again, there is no evidence that planet migration or growth substantially affects the disk-planet torques for the parameters adopted in these models. Furthermore, there is no evidence for strong coorbital torques dominating planet's migration.

In carrying out calculations at higher disk masses, we have introduced a possible inconsistency between the orbital motion of the disk and the planet. The orbital motion of the planet is affected by the axisymmetric gravitational force of the disk. On the other hand, the motion of the disk near the planet is not affected by this force, since disk self-gravity is ignored. This difference in rotation rates can lead to an artificial increase in the planet migration rate (Pierens & Huré 2005; Baruteau & Masset 2008). This issue has some quantitative effect on our results in this section. But, the qualitative results (approximately following the expectations of standard Type I and II theory) remain. We examine this issue further in Appendix C.

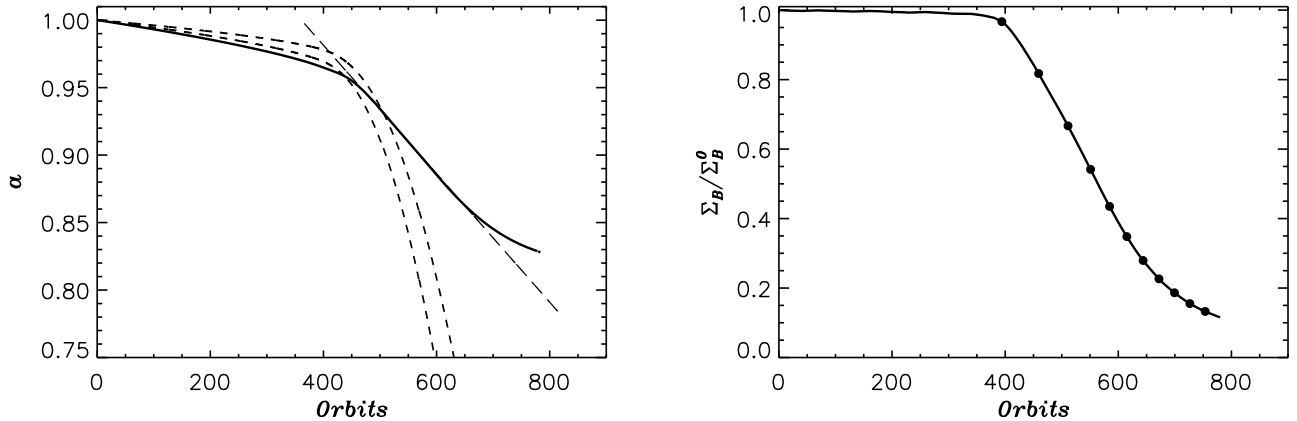


FIG. 9.— *Left*: Same as left panel of Figure 6, but for a disk with ten times the turbulent kinematic viscosity ($\nu = 1 \times 10^{-4} a_0^2 \Omega_0$ or $\alpha = 0.04$), same H/r , and initial Σ_p . As in Figure 6, the upper (lower) short-dashed line is for unsaturated (saturated) coorbital torques, using the mass evolution shown as a short-dashed curve in Figure 5. The long-dashed line representing Type II migration has a slope equal to $-0.7\nu/a$. *Right*: Average disk density near the planet relative to the local initial (unperturbed) value as a function of time, as in the right panel of Figure 6. Solid circles mark times when M_p/M_s is 5×10^{-5} ($M_p = 16.7 M_E$) or an integer multiple of 2×10^{-4} ($M_p = 66.6 M_E$).

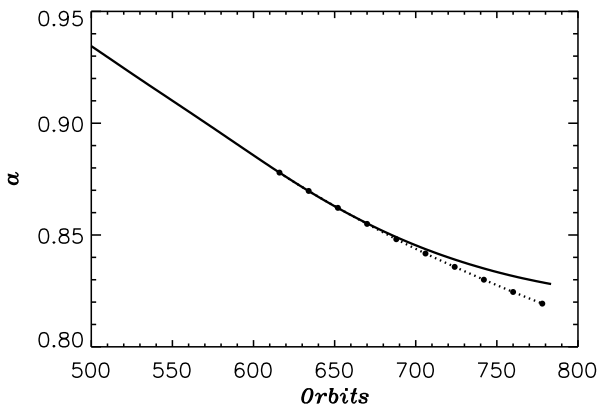


FIG. 10.— Comparison of radial migration obtained from the simulation on the left panel of Figure 9 (solid line) with that obtained from a similar three-dimensional simulation (dotted line with solid circles) with a fixed mass planet $M_p = 1 M_J$ (see text for further details).

4.2. Higher Initial Planet Mass

We have shown that if a low mass protoplanet is allowed to rapidly grow in mass while it migrates, the orbital radius evolution begins at the Type I rate (eqs. 17 and 18) and approaches the Type II migration rate as a clean gap develops. Since the evolving planet gains mass at the fastest possible rate, the run-away accretion rate, the time available for gap clearing is relatively short. Such conditions should be favorable for migration dominated by coorbital torques. But as we saw in Figure 11, such situations only reveal Types I and II migration. In this section, we explore a more extreme situation for providing coorbital material. We consider the case that a planet of higher initial mass (higher than the $5 M_E$ considered thus far) is suddenly immersed in a smooth disk. Gap clearing is then not initially present for the higher mass planets. More coorbital gas is available for affecting migration.

We consider a planet with initial mass $M_p = 0.3 M_J$

($M_p/M_s = 3 \times 10^{-4}$) that is allowed to grow and migrate in a three-dimensional disk with initial density $\Sigma_p \approx 300 \text{ g cm}^{-2}$ at $a_0 = 5.2 \text{ AU}$ (same as the lower initial density disk in Fig. 11), $H/r = 0.05$, and $\nu = 1 \times 10^{-5} a_0^2 \Omega_0$. Its orbital radius evolution is plotted as a dotted curve with solid circles in Figure 13, together with the migration track of the model that starts with $M_p = 5 M_E$ at $t = 0$ (plotted as a solid curve). For purposes of comparison, the initial orbital radius a_0 for the dotted curve case is chosen to be the a value of the solid curve case when its planet mass is also $0.3 M_J$. Given the large initial mass of the planet for the dotted curve case, the mass growth is very rapid: the planet gains about $0.7 M_J$ over the first ~ 50 orbits of evolution. The figure shows that, with these disk conditions, migration rates differ only for a brief period of time, but they soon converge to values compatible with orbital migration in the more relaxed disk (compare slopes of solid and dotted lines). The dashed lines in the figure show that the planet initially migrates at the Type I rate⁵. But it later slows to nearly the same rate as the solid curve case. Again, there is no indication of Type III migration.

4.3. Nongrowing Planets in a Colder Disk

We consider the case of a nongrowing $0.3 M_J$ planet by removing gas mass near the planet without adding the mass of this material to the planet's mass. This situation may mimic the effects of an efficient disk wind. These models differ from those in MP03 and DBL05, who considered nonaccreting planets, only with respect to the accretion boundary conditions near the planet and the time of planet release.

Unlike the mass removal case, the nonaccreting case may introduce a complication because of the buildup of gas within the planet's Hill sphere, which can become more massive than the planet. It has been argued that inertia effects from material close to the planet could introduce complications in self-consistently analyz-

⁵ Note that, for a constant mass planet and $\Sigma_p \propto a^{-1/2}$, it follows that $|\dot{a}_I| \propto a$ (see eq. 17).

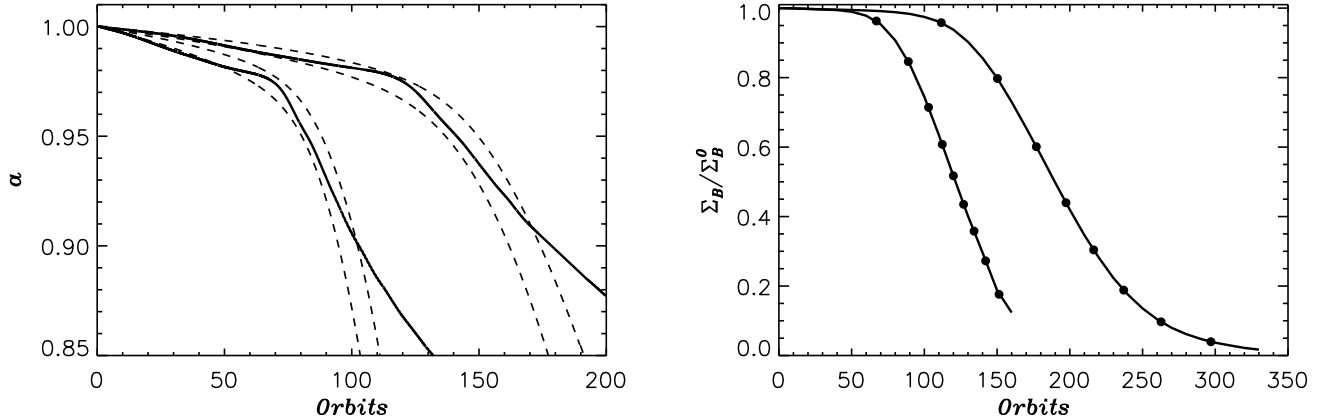


FIG. 11.— *Right:* Orbital evolution under the same conditions as the model in Figure 6, but with higher disk densities. *Solid curves:* Simulation results for orbital migration of a planet in a three-dimensional disk with initial surface density equal to $\Sigma_p = 9 \times 10^{-4} M_s a_0^{-2}$, or about 300 g cm^{-2} at $a_0 = 5.2 \text{ AU}$ (upper migration track), and $\Sigma_p = 1.5 \times 10^{-3} M_s a_0^{-2}$, or about 500 g cm^{-2} (lower migration track). *Dashed curves:* Predicted orbital migration according to Type I theory, equations (17) (*upper curve* of pair for unsaturated coorbital torques) and (18) (*lower curve* of pair for saturated coorbital torques). *Right:* Average disk density near the planet relative to the local initial (unperturbed) value as a function of time, as in the right panel of Figure 6. Solid circles mark times when M_p/M_s is 5×10^{-5} ($M_p = 16.7 M_E$) or an integer multiple of 2×10^{-4} ($M_p = 66.6 M_E$).

ing the dynamics of the system (Papaloizou et al. 2007). Appendix D describes some effects of the nonaccreting boundary condition. To avoid this potential problem, we remove gas near the planet and ignore torques exerted by the gas on the planet within the inner half of the Hill sphere (by radius), where most of the bound gas resides (see Fig. 29).

We are interested in seeing whether these situations could give rise to strong torques outside the Hill sphere that cannot be accounted for by Type I or Type II theory in the case of a planet of fixed mass. As we show below, there are conditions under which such strong torques occur in the coorbital region.

4.3.1. Simulations Setup

We consider a Saturn mass ($0.3 M_J$) planet in a disk having $H/r = 0.03$. The initial (unperturbed) disk surface density varies as $\Sigma = \Sigma_p(a_0)(a_0/r)^{3/2}$, with $\Sigma_p(a_0) = 2 \times 10^{-3} M_s a_0^{-2} \approx 670 \text{ g cm}^{-2}$, and kinematic viscosity $\nu = 1 \times 10^{-5} a_0^2 \Omega_0$. Most of these calculations are carried out in two dimensions since $R_H \simeq 1.5 H$. However, we checked that results from three-dimensional models are in general agreement with those from two-dimensional models (see *dotted curves* in Fig. 14). Simulations in three dimensions use the grid system outlined in section 3. As in the three-dimensional case, the two-dimensional grid has a linear base resolution of $0.014 a_0$. In the coorbital region around the planet, the linear resolution is $0.02 R_H$. Since we intend to study some global properties of flow dynamics in the coorbital region, three grid levels extend 2π in azimuth around the star. Convergence tests at these grid resolutions are presented in Appendix D.

As anticipated above, here we assume that some process removes gas from the disk, according to the procedure detailed in section 3.1.1, but that the planet mass remains constant. The migration rate of the fixed mass planet is not substantially affected by the assumption that the gas is removed. In Appendix D we show that

configurations with a nonaccreting planet result in similar migration tracks. Hence, our conclusions would apply to nonaccreting planets as well.

In MP03 and DBL05, the planet’s orbital radius was initially fixed for over 470 orbits, so that a time-steady disk gap would form before it underwent migration. Here we reconsider that configuration, but examine cases where the planet’s initial orbital radius is fixed for a shorter time, only 100 orbits. This case is somewhat like that of section 4.2 which has more gas in the coorbital region (*lower curve* case in Fig. 11), but instead has a fixed mass planet in a cooler disk. The following factors applied here should help increase the torques from the coorbital region: cooler disk, fixed planet mass, higher disk density, and reduced time on initially fixed orbit.

4.3.2. Results

Figure 14 shows that the migration timescale of the planet is quite short and that it lengthens as the release time increases (and the gap deepens). We focus on the case with $t_{\text{rls}} = 100$ (*solid line* case in the figure), which has a migration timescale of order 100 initial orbital periods. Although short, this migration timescale is longer than the Type I migration timescale that would be predicted if the planet did not open a gap (*lower short-dashed curve* of pair⁶). The planet does open a partial gap, as seen in Figure 15. So it might appear that a weakened form of Type I migration, due to partial gap opening, could explain the simulated migration rate. However, we demonstrate below that the migration cannot be explained by the usual Type I theory.

Figure 16 shows the torque distribution per unit disk mass exerted on the planet, as defined by equation (8). The torque density distribution at the time of release of the planet, 100 orbits after the start of the simulation, reveals a curve characteristic of Type I torques.

⁶ Note that, for a constant mass planet and $\Sigma_p \propto a^{-3/2}$, it follows that \dot{a}_I is a constant (see eq. 17).

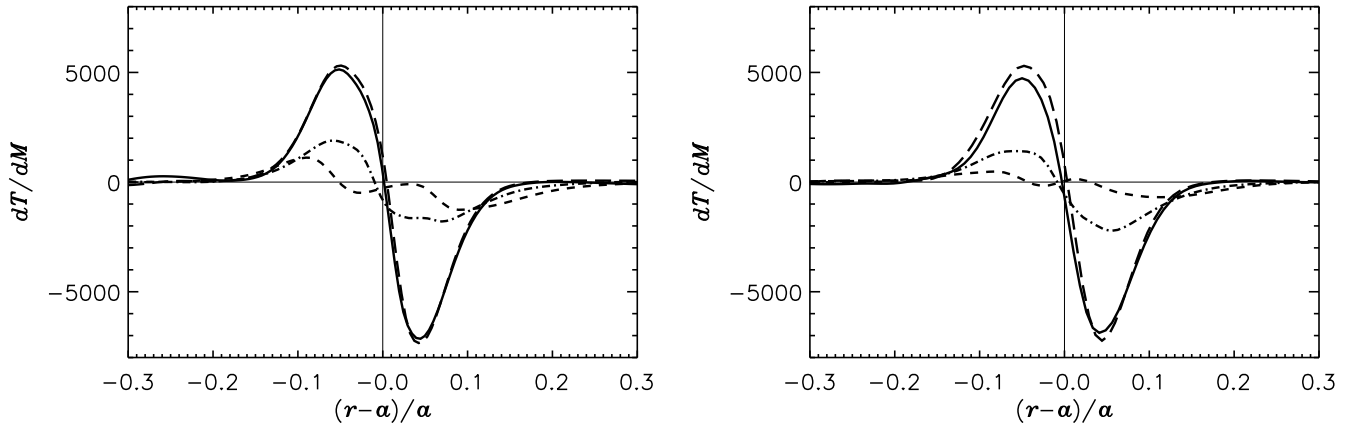


FIG. 12.— Torque per unit disk mass on the planet as a function of normalized distance for the migrating and growing planets plotted in Figure 11. *Left*: Case with initial surface density at the initial orbit of the planet equal to $\Sigma_p \approx 300 \text{ g cm}^{-2}$. *Right*: Case with initial surface density at the initial orbit of the planet equal to $\Sigma_p \approx 500 \text{ g cm}^{-2}$. The vertical scale is in units of $GM_s(M_p/M_s)^2/a$, where $a = a(t)$. The solid, long-dashed, dot-dashed, and short-dashed curves refer to times when $M_p = 6.0 M_E$, $9.3 M_E$, $0.36 M_J$, and $1.0 M_J$, respectively.

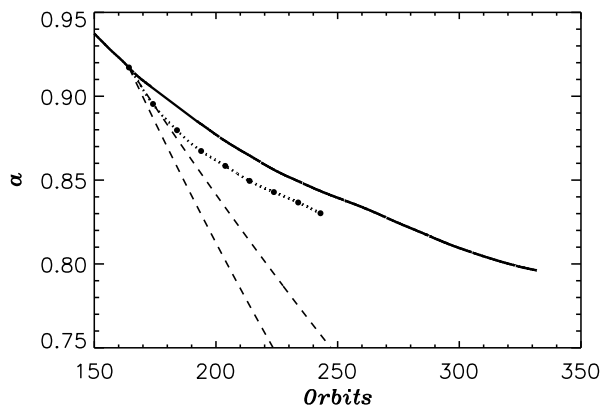


FIG. 13.— Migration with different initial conditions. *Solid curve*: Orbital radius evolution of a planet with initial mass $M_p = 5 M_E$ that interacts with a three-dimensional disk having initial surface density at the planet’s initial radial position $\Sigma_p \approx 300 \text{ g cm}^{-2}$ at $a_0 = 5.2 \text{ AU}$ (same as the upper migration track plotted in Fig. 11). It has mass $M_p = 0.3 M_J$ at a time of about 165 orbits (see Fig. 3, *dashed line*), when $a \simeq 0.92 a_0$. *Dotted curve with solid circles*: Orbital radius evolution of a planet with initial mass $M_p = 0.3 M_J$ that interacts with the same initial unperturbed disk density distribution as the solid curve case has at time $t = 0$. The planet starts at the same radius ($a \simeq 0.92 a_0$) as the solid curve where that planet has acquired a mass of $0.3 M_J$. The difference in the two cases is that the solid curve case has a partially cleared gap when $M_p = 0.3 M_J$ (see Fig. 11, *right panel*), while the dotted curve case starts in a smooth unperturbed disk. *Dashed curves*: Orbital radius evolution of a planet according to Type I theory (eq. 17 and 18) for a planet of fixed mass $M_p = 0.3 M_J$ (*lower curve* of pair for saturated coorbital torques) and disk density at $r = 0.92 a_0$ for the unperturbed initial disk.

The distribution is similar to the cases plotted in Figure 1, although it is somewhat larger in magnitude, as expected by the lower sound speed of the gas and the two (rather than three) dimensions of the simulation. However, at later times the torque distribution changes character, with much larger values in the coorbital zone, within radial distances of about $2R_H \simeq 0.1 a(t)$ from the orbit of the planet. In particular, there is substantial torque occurring in the radial band $|r - a| < R_H$, where $R_H = 0.046 a$. We argued in section 2.2.2 that

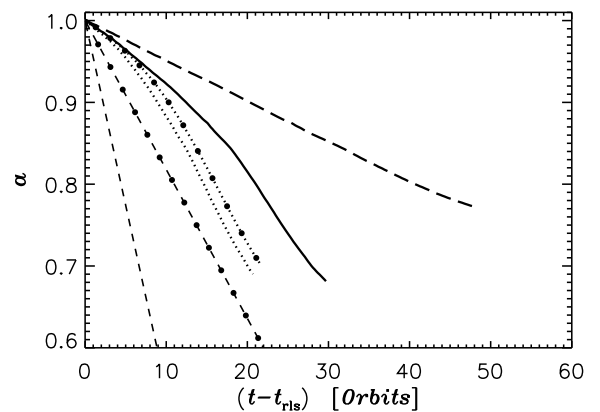


FIG. 14.— Orbital migration of a Saturn-mass planet of fixed mass ($M_p = 0.3 M_J$) in a cold ($H/r = 0.03$) and high mass disk ($\Sigma_p \approx 670 \text{ g cm}^{-2}$ at the planet’s initial position). Mass is removed from the disk near the planet to prevent a mass buildup there. The planet is embedded in a two-dimensional disk and held on a fixed orbit for $t_{\text{rls}} = 50$ (*dotted lines*), 100 (*solid line*), and 200 (*long-dashed line*) initial orbital periods. The dotted line with solid circles plots the migration track from a three-dimensional disk model with $t_{\text{rls}} = 50$ orbits. The orbital radius is in units of a_0 . For $a_0 = 5.2 \text{ AU}$, the unit of time is ≈ 12 years. The predicted Type I migration tracks, assuming the planet does not open a gap, are plotted for a two-dimensional (*short-dashed line*) and a three-dimensional (*short-dashed line with solid circles*) disk.

this region involves only coorbital torques (not Lindblad torques). We have verified that this torque is not originating from within the planet’s Hill sphere (see Fig. 27). The contribution from within the Hill sphere is about 20% of the net torque at release time and generally less than about 10% at later times.

Figure 15 shows that the planet is migrating on a shorter timescale than that of gap opening. At release, the planet is fairly symmetrically positioned in the gap. Later, the planet lies much closer to the inner edge of the gap than to the outer edge, and the gap is less deep. Such a situation would be expected to lead to slower or even outward migration according to Type I theory of Lindblad resonances, since the inner resonances (which

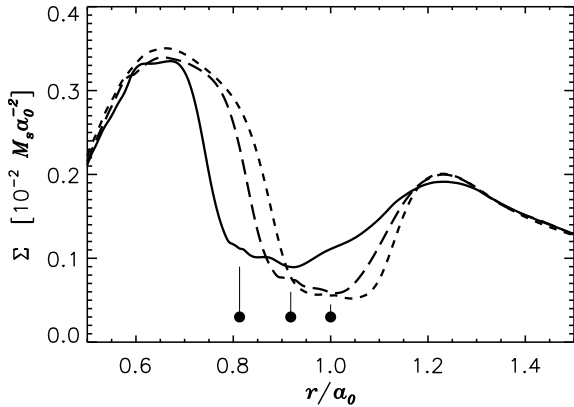


FIG. 15.— Axisymmetric radial density distribution $\Sigma(r, t)$, of a disk containing a Saturn-mass planet ($M_p = 0.3 M_J$), plotted as a function of radius at 3 times: the time of planet release $t_{\text{rls}} = 100$ initial orbital periods (short-dashed line), $t_{\text{rls}} + 10$ initial orbital periods (long-dashed line), and $t_{\text{rls}} + 20$ initial orbital periods (solid line). The solid circles mark the planet orbital radii at these times, as the planet migrates inward.

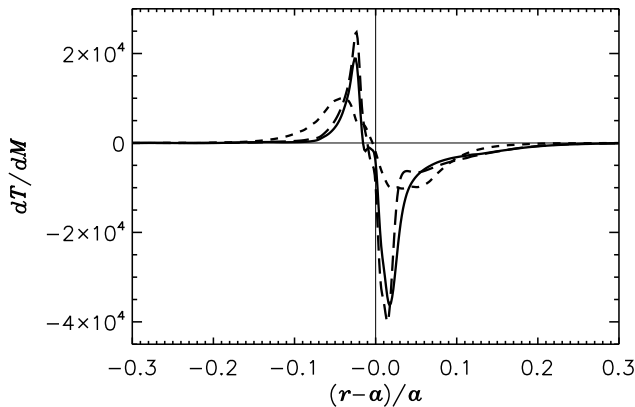


FIG. 16.— Torque per unit disk mass on a Saturn-mass planet ($M_p = 0.3 M_J$) in units of $G M_s (M_p/M_s)^2/a(t)$ as a function of the normalized distance from the planet, undergoing fast migration, at 3 different times: the time of planet release $t_{\text{rls}} = 100$ initial orbital periods (short-dashed curve), $t_{\text{rls}} + 10$ initial orbital periods (long-dashed curve), and $t_{\text{rls}} + 20$ initial orbital periods (solid curve).

provide outward migration) are more strongly activated than the outer resonances (which provide inward migration) due to the asymmetric density distribution near the planet. In fact, the slowing/stalling of inward migration due to the feedback from the inward disk density of a migrating planet was envisioned by Hourigan & Ward (1984) and Ward & Hourigan (1989) in their consideration of the inertial limit to planet migration. To quantify the effects of standard Type I torques, we apply the Type I torque distribution taken at the time of planet release in Figure 16. In doing so, we are ignoring pressure effects on dT/dM due to the changing gap shape. We determine the Type I torques at the later times by integrating this torque distribution (appropriately shifted to the instantaneous position of the planet) over the disk mass distributions in Figure 15. The torque is then given

by

$$T_I(t) = 2\pi \int \frac{dT}{dM}(x, t_{\text{rls}}) \Sigma(r, t) r dr \quad (20)$$

where $x = (r-a)/a$ and $a = a(t)$. We find that the resulting Type I migration rates at times of 10 and 20 orbits after release are *outward* and equal to $\dot{a} = 2 \times 10^{-4} a_0 \Omega_0$ and $4 \times 10^{-5} a_0 \Omega_0$, respectively. Clearly, results from the simulation are not consistent with the expectations of the usual Type I migration theory. Instead, we claim the effects of the corotation resonances are critical for migration here.

In the model by OL06, fast migration is due to torques caused by a density asymmetry in the coorbital region between gas on the leading and trailing sides of the planet. The gas on the leading side of the planet is trapped and contains gas acquired at other radii, while the trailing side contains ambient gas near the planet. The contrast between the trapped and ambient gas is limited by viscous diffusion. The trapped gas is in a quasi-steady advective-diffusive equilibrium. The density asymmetry and thus the torque is caused by the motion of the planet.

To test this model, we analyzed streamlines in the coorbital region in the frame comoving with the planet. We determine the streamlines in the simulations by following the motion of tracer particles that move with the velocity of the gas (see Appendix D.1). In Figure 17 we plot coorbital streamlines near before the planet is released, i.e., while the planet was on a fixed stationary orbit. The figure shows good agreement between the simulation and theory. The streamlines are symmetric between the leading ($\phi > \phi_p$) and trailing ($\phi < \phi_p$) sides of the planet. Figure 18 shows the streamlines after the planet is released, while the planet is migrating. Strictly speaking, these are not streamlines in the simulation case but trajectories, since the flow is not in a strict steady state in the comoving frame of the planet because the planet is migrating at a variable rate. The theoretical streamlines depend on the planet-to-star mass ratio and the migration rate of the planet. They are calculated assuming a steady state and constant migration rate by means of the linear perturbation model of OL06. The theoretical streamlines were calculated by using intermediate parameter values from the simulation during the interval of planet migration: $\dot{a} = -0.002 a_0 \Omega_0$ and $r = 0.85 a_0$. The simulated and theoretical streamlines in Figure 18 are in approximate agreement. They show closed streamlines on the leading side of the planet's azimuthal motion. They contain the trapped gas described above. The open streamlines on the trailing side of the planet involve ambient gas that streams outward past the planet. The smaller closed streamlines are centered at about the same azimuth in the two plots, about 0.2π ahead of the planet. Figure 19 shows that the gas density asymmetry in the coorbital region between the leading and trailing sides of the planet increases with time. The unperturbed background density increases with time as the planet encounters higher density gas in its inward migration. Notice that the density increase is higher on the trailing side of the planet than on the leading side. This result suggests that the trapped gas approximately retains its initial density as the planet migrates. The gas on the trailing side more fully reflects the local density. The density asymmetry then gives rise to the dominant

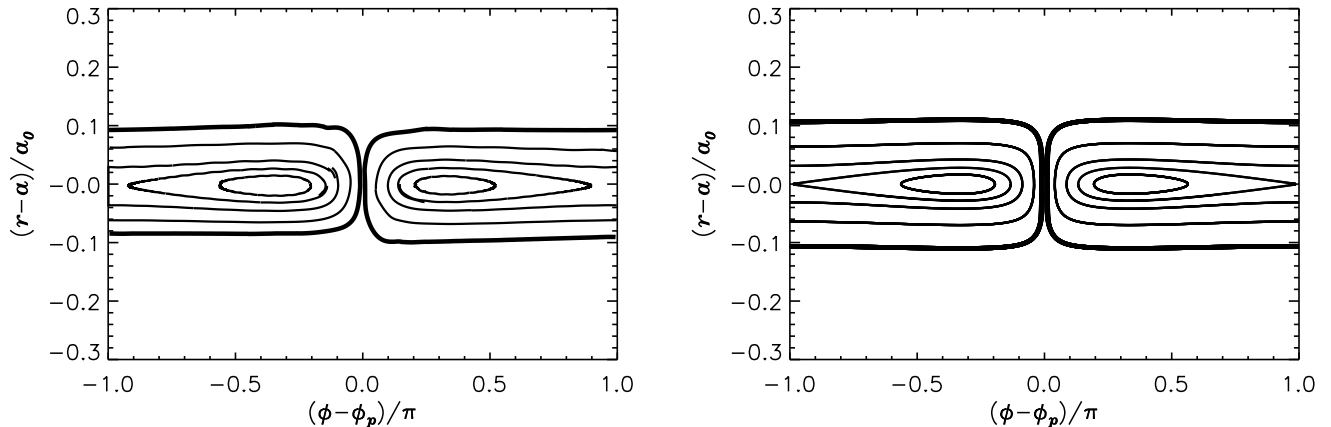


FIG. 17.— Trajectories of gas in the coorbital region near a Saturn-mass planet ($M_p = 0.3 M_J$) on a fixed circular orbit with orbital radius $a = a_0$. The trajectories are determined in the comoving frame of the planet, which is located at the origin. Disk properties are the same as in Figure 14. The left panel shows the results of our simulation and the right panel shows results given by a theoretical model (OL06).

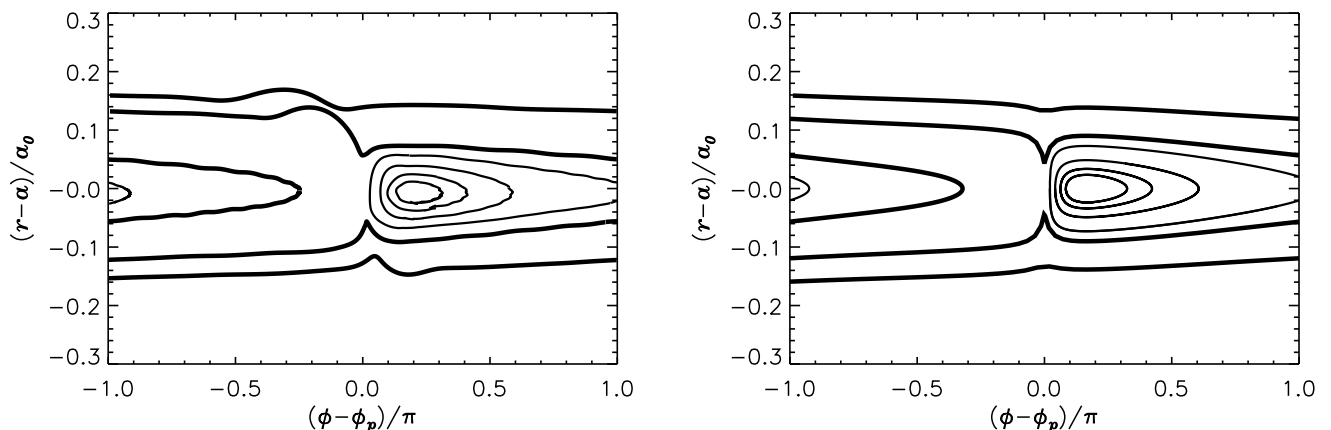


FIG. 18.— Trajectories of gas in the coorbital region near a Saturn-mass planet undergoing fast migration (solid curve in Fig. 14). The trajectories are determined in the comoving frame of the planet, located at the origin. The thicker lines denote open trajectories that pass by the planet. The thinner lines denote closed trajectories containing trapped gas. Results from the simulation are presented in the left panel and results from a theoretical model (OL06) are displayed in the right panel.

torque on the planet.

The OL06 model does not determine the value of coorbital corotational torque for a migrating planet. It does provide a detailed analysis for the noncoorbital corotational torque. In that case, the effect of migration is to amplify the standard coorbital torque for a nonmigrating planet (Goldreich & Tremaine 1979). By analogy, one might expect similar behavior in the coorbital case. The standard torque is proportional to the radial derivative of $\Sigma(r)/B(r)$, and hence of the disk vortensity $-2B(r)/\Sigma(r)$, where $\Sigma(r)$ is the disk axisymmetric surface density (azimuthally averaged surface density) and $B(r)$ is the Oort constant. In the unperturbed disk model considered here, the vortensity is constant, and so the coorbital torque is predicted to be zero. However, the gap structure in the disk modifies the surface density $\Sigma(r)$ near the planet (see Fig. 15), thereby providing a vortensity gradient.

4.4. Conditions for Type III Migration

The results in section 4.3.2 provide evidence for migration dominated by coorbital torques, or Type III migration. Within the framework of the OL06 model we generalize the results of the simulations and describe some conditions that are favorable for Type III migration.

As in section 4.3.2, we consider a planet of fixed mass. For a planet whose mass is large enough to open a gap, we apply the initial condition that the planet undergoes migration before steady gap formation completes, as was the case in section 4.3.2.

We require that the planet does not strongly deplete the gas in the coorbital region as it migrates. This requirement implies that the migration timescale across the coorbital region be shorter than the timescale to clear a gap over that region. Figure 15 demonstrates that this condition holds for the model in section 4.3.2.

To derive a crude estimate for this condition, we assume that the torques exerted by the planet lead to a local change in disk angular momentum over a region whose size is comparable to the coorbital region. Each one-sided torque (interior and exterior to the orbit of the

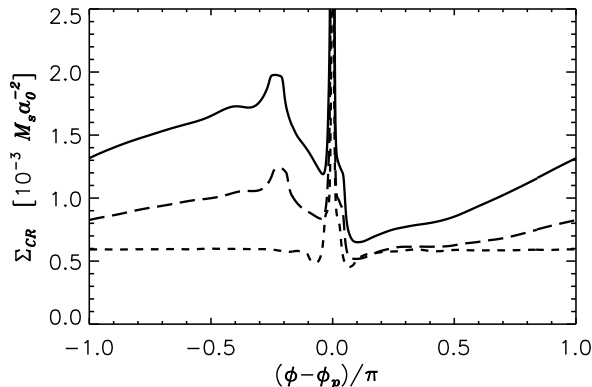


FIG. 19.— Radial average of the surface density within the coorbital region (defined as having radial extent $2R_H \simeq 0.1a(t)$ of the planet’s orbit) as a function of azimuth at 3 different times: the time of planet release $t_{\text{rls}} = 100$ initial orbital periods (*short-dashed line*), $t_{\text{rls}} + 10$ initial orbital periods (*long-dashed line*), and $t_{\text{rls}} + 20$ initial orbital periods (*solid line*).

planet) on the gas is capable of clearing a gap, while the net effect of both interior and exterior torques results in migration. The condition that the gap clearing timescale is longer than the migration timescale becomes

$$M_c \gtrsim \frac{M_p}{A}, \quad (21)$$

where M_c is the mass of the coorbital region and A is the dimensionless torque asymmetry

$$A = \frac{|T_e| - |T_i|}{|T_e|}, \quad (22)$$

where T_i and T_e denote the torques interior and exterior to the planet’s orbit, respectively.

Another condition is that the migration rate be large enough that there is a strong asymmetry in streamlines between the leading and trailing sides of the planet, as seen in Figure 18. According to OL06, the asymmetry is strong for migration rates greater than $|\dot{a}_A| = 1.45 \Omega a M_p / M_s$. Since the migration begins as Type I migration (see *short-dashed line* in Fig. 16), the condition is that $|\dot{a}_I| \gtrsim |\dot{a}_A|$. This condition is approximately

$$\Sigma_p \gtrsim \frac{M_s}{a^2} \left(\frac{H}{a} \right)^2. \quad (23)$$

Notice that the condition is independent of planet mass, since both \dot{a}_I and \dot{a}_A are linear in the planet mass.

We now apply these conditions to the model simulated in section 4.3.2. The asymmetry parameter is estimated as $A \approx 0.3$, from the initial torque distribution in Figure 16. Condition (21) is then satisfied for this model, since $M_c \approx 7 M_p$. Condition (23) is also (marginally) satisfied, since the initial density is $\Sigma_p a^2 / M_s = 2 \times 10^{-3}$ and $(H/a)^2 = 9 \times 10^{-4}$. None of the other models discussed in this paper satisfy both conditions.

It also appears that the condition that the planet mass is fixed (or slowly increasing) is important. The dashed curve on the right panel of Figure 27 in Appendix D suggests that a planet that grows in mass at the run-away rate would not undergo rapid migration long enough to move very far. The slow-down is partly due to gap opening that reduces the torques.

The picture is then that a fixed mass planet, initially undergoing sufficiently fast Type I migration, develops strong coorbital torques due to asymmetric trapped gas. The situation is not simple, however. We saw in section 4.3.2, that the disk’s feedback to the planet’s motion might slow or halt Type I migration, but the coorbital torques allow the inward migration to continue. We found that the rate of the resulting migration is actually slower than Type I migration for a smooth disk. So the conditions (21) and (23) are suggestive only at this point and require further testing.

5. SUMMARY AND DISCUSSION

We have analyzed the evolution of migrating planets that undergo run-away gas accretion by means of multi-dimensional numerical simulations. The results agree with the predictions of Type I and Type II migration (see Figures 6 through 9) for a planet of time-varying mass that we obtain from simulations. The set of simulations include cases with disk densities as low as the minimum mass solar nebula value and as high as 5 times that value, viscosities $\alpha \approx 0.004$ and 10 times that value (also 50 times that value, $\alpha \approx 0.2$, in a test reported in Appendix B), disk temperatures corresponding to $H/r = 0.05$ and a colder case of $H/r = 0.04$. The mass accretion rates onto the planet (see Figures 3 and 5) are in general agreement with previous determinations based on fixed mass planets on fixed circular orbits, when comparing cases with the same planet mass and disk properties for which the growth timescale is longer than the gap opening timescale. Planet mass growth rates can be understood in terms of accretion within the Bondi radius at lower planet masses, accretion within the Hill radius at intermediate masses, and accretion through the gap at higher planet mass (see Fig. 4). Mass growth rates typically peak at the intermediate planet masses, a few tenths of a Jupiter mass.

An important diagnostic for the nature of the disk-planet torques is the scaled torque density distribution per unit disk mass as a function of the scaled radial distance from the planet. In the linear regime of the standard theory of disk-planet resonances, for a fixed form of the disk density distribution $d \ln \Sigma / d \ln r$ and gas properties (sound speed and viscosity), this scaled torque distribution should be universal, independent of planet mass and disk density value. We verified this universality for low mass planets, although the distribution varies somewhat with planet mass for larger mass planets that open gaps (compare low mass cases in Figures 1, 7, and 12).

There is no fundamental distinction between the torques involved in Type I and Type II migration. This follows from the near independence of the scaled torque density distribution with planet mass. Previous concepts of Type II suggested that a planet in a clean gap would migrate inward like a test particle that follows the disk accretion. Here we describe a view for cases where the gap is not completely clear of material. The difference in Type I and Type II rates is due to the mass density distribution of the gas that multiplies torque density in determining the torque on the planet. In Type II migration, the density distribution adjusts so that the net torque on the planet causes it to migrate at approximately the viscous evolution rate of the disk. The transition between the two forms of migration is quite smooth.

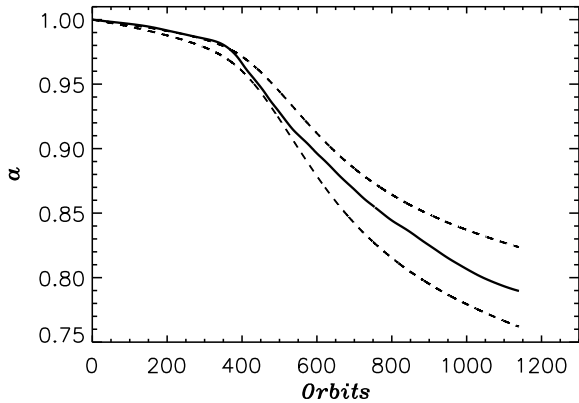


FIG. 20.— Orbital migration of a planet undergoing run-away gas accretion. Orbital radius in units of a_0 (5.2 AU), as a function of time in units of the initial orbital period (≈ 12 years). The initial planet mass is $5 M_E$. The initial surface density is $\Sigma_p = 3 \times 10^{-4} M_s a_0^{-2} \approx 100 \text{ g cm}^{-2}$ at the planet’s initial orbital radius and $H/r = 0.05$. *Solid curve*: Results from the same simulation as in Figure 6 for a migrating, mass-gaining planet. *Short-dashed curves*: Predictions based on Type I migration theory, obtained by solving equations (17) and (18), taking into account the time variable mass of the planet (Fig. 3, *solid line*) and roughly accounting for the gas depletion near the planet (see text). The upper (lower) dashed curve is for migration with unsaturated (saturated) coorbital torques.

To illustrate this point, we plot in Figure 20 the orbital evolution of the planet through the phase where gap formation sets in. The figure shows that the migration rate can be accounted for by standard Type I theory, corrected for the gas depletion in the gap region, although there is no unique prescription to do this. In the figure, the theoretical curves (*dashed lines*) are determined by Type I migration theory, equations (17) and (18), with the density Σ taken to be the average value in a radial band of half-width $0.15 a$ (a typical gap width) centered on the planet.

For a given planet mass, the torque density diagnostic reveals that the distribution is not strongly affected by migration or accretion (Figure 1 is quite similar to Figures 7 and 12 for similar planet masses). In particular, there is no evidence for strong coorbital torques. However, in a certain case, we do find evidence for strong coorbital torques, or Type III migration. This case has a planet of fixed mass, $0.3 M_J$, that is immersed into a cold, smooth disk. The planet is held at a fixed orbit for relatively short time (~ 100 orbits) before being released, so that gap clearing is incomplete. The torque distribution at the time the planet is released follows the expectations of the standard theory for nonmigrating planets. This can be seen by comparing the curve for the $0.3 M_J$ case in Figure 1 (*dot-dashed curve*) with the short-dashed curve (time $t = t_{\text{rls}}$) in Figure 16. (There are differences in the magnitude of the distributions because of differences in gas sound speeds and dimensionalities of the calculations, but the forms of the distributions are similar). At later times, Figure 16 reveals a transition to a completely different torque distribution, where coorbital torques play a critical role.

The strong coorbital torque can be understood in terms of an asymmetry in the streamlines between the leading and trailing sides of the planet, in accord with the an-

alytic model of OL06 (see Figures 17 and 18) and also along the lines of Artymowicz (2004). This asymmetry causes trapped material to persist on the leading side of the planet which has a different density from the ambient gas that flows on the trailing side (see Fig. 19). The asymmetry gives rise to the coorbital torque. We suggest some criteria for this form of migration (see section 4.4). More exploration is needed to test them.

Although we find evidence for Type III migration, the conditions required appear somewhat artificial, i.e., incomplete gap clearing (nonequilibrium gap) of a cool disk with a planet of fixed mass. It is not clear whether and/or how conditions for Type III could arise in a more plausible evolution scenario.

We have generally assumed that the planet is able to accrete almost all gas the disk is able to provide (so-called run-away gas accretion). For a disk viscosity $\nu \gtrsim 1 \times 10^{-5} a_0^2 \Omega_0$, the mass accretion rates are large. The time to build a $1 M_J$ planet starting with a $5 M_E$ planet in a minimum mass solar nebula is shorter than $\sim 10^5$ years, substantially less than the observationally determined disk lifetimes of $\sim 10^6$ years (Haisch et al. 2001; Flaherty & Muzerolle 2008). Over this 10^5 year time interval, the planet has radially migrated inward by only $\sim 20\%$ of its initial radius. In other words, for these models, the mass doubling timescale for a $M_p \lesssim 1 M_J$ planet is short compared to the migration timescale and the disk lifetime. This situation stands in strong contrast to the earlier phases of planet formation where the migration timescales are shorter than the planet mass doubling timescales and disk lifetimes (e.g., Ward 1997; Hubickyj et al. 2005).

The run-away accretion rates pose some challenges for explaining the mass distribution of planets (Butler et al. 2006). Typical accretion rates in T Tauri stars are $\sim 1 \times 10^{-8} M_\odot$ per year (Hartmann et al. 1998). For a steady-state unperturbed disk (without a planet), the accretion rate is given by $3\pi\nu\Sigma$. The initial disks considered in this paper are not in a steady state, but this accretion rate provides a reasonable estimate. For the minimum mass nebula model (Fig. 3), the kinematic turbulent viscosity we typically adopt, $\nu \sim 10^{-5} a_0^2 \Omega_0$, was chosen so that the accretion rate evaluates to about this same value, $\sim 1 \times 10^{-8} M_\odot$ per year. In the case of a planet embedded in a disk, if there is a comparable accretion rate onto a planet of mass $M_p \lesssim 1 M_J$ (as found by Lubow & D’Angelo 2006), then the mass doubling timescale for a Jupiter-mass planet is about 10^5 years, consistent with what we found in the simulations in this paper. But then it is not at all clear why planets would not almost always achieve masses higher than $\sim 1 M_J$, in contradiction with the observed mass distribution of extra-solar planets and the case of Saturn. Special timing for disk dispersal could be invoked, but may be artificial.

There are a few possible explanations. A colder disk ($H/r < 0.05$) would experience stronger tidal truncation effects from a Jupiter-mass planet, as H becomes significantly smaller than $R_H \simeq 0.07 a$. This effect could certainly reduce the accretion rate by a large enough factor (say 10), so that the mass doubling timescale for a $\sim 1 M_J$ planet would become of order 10^6 years, consistent with the suggestion by Dobbs-Dixon et al. (2007). The issue then is how cold the disk would need to be. The model in this paper with $H/r = 0.04$ (Fig. 5, *long-*

dashed line) has the same unperturbed overall disk accretion rate as the $H/r = 0.05$ case (Figures 3 and 5, *solid line*), since ν and the initial surface density $\Sigma(r)$ are the same. The accretion rate onto the planet from the colder disk ($H/r = 0.04$) differs from the case with $H/r = 0.05$ by only 10%. Model *h* in Lubow & D'Angelo (2006) for a nonmigrating planet of fixed mass, having $H/r = 0.03$, has an accretion rate that is $\sim 25\%$ less than model *b*, which has $H/r = 0.05$ and the same unperturbed overall disk accretion rate. Consequently, in this disk thickness range ($0.03 \leq H/r \leq 0.05$), we find that the reduction in the accretion rate onto the planet due to cooler disks is not significant. For higher mass planets ($5\text{--}10 M_J$), we expect that the accretion rate will be reduced by tidal truncation effects to a level where the planet mass doubling timescale is comparable to the disk lifetime, as found in previous studies of planets on fixed orbits (Lubow et al. 1999; Bate et al. 2003; D'Angelo et al. 2003). This effect may set the upper limit to planet masses.

Another possibility is that there is a feedback effect that limits the gas accretion rate. Perhaps the heating of the protoplanet envelope by impacting solids continues to later times than is assumed in the standard core accretion model. Depletion of disk solids near the planet occurs in the standard core accretion model, when planet migration is not included. With migration, it is possible that continued accretion of disk solids would occur (e.g., Alibert et al. 2005), resulting in continued heating that could limit the gas accretion rate further. It is not clear how well this possibility works, since planetesimals will

get trapped into resonances as the planet migrates (Zhou & Lin 2007). Having a higher mass solid core is problematic in the case of Jupiter, whose solid core mass is thought to be a small fraction of the total mass (see Guillot 2005 and discussion in Lissauer & Stevenson 2007). It is also possible that winds emanating from the circumplanetary disk within the planet's Hill sphere could reduce the accretion rate onto the planet. Magnetically driven winds are believed to play an important role in the case of young stars (Blandford & Payne 1982; Pudritz & Norman 1986; Shu et al. 1994). There are likely differences in the flow properties from the stellar outflow case (Fendt 2003). However, it is not clear that the winds would be able to expel a large enough fraction (say 90%) of the accreting gas to sufficiently reduce the accretion rate onto the planet.

We thank Hui Li and Doug Lin for discussions about Type III migration. We also thank the referee for providing prompt and useful comments. GD is supported through the NASA Postdoctoral Program. SL acknowledges support from NASA Origins of Solar Systems grants NNG04GG50G and NNX07AI72G. We acknowledge computational facilities supported by the NASA High-End Computing Program systems under grants SMD-07-0372 and SMD-08-0582.

Facilities: NAS: NASA Advanced Supercomputing Division (Columbia/Schirra); NCCS: NASA Center for Computational Sciences (Palm/Explore).

APPENDIX

A. NUMERICAL SENSITIVITY STUDY

We conducted several tests to assess the sensitivity of the results presented in section 3 to the choice of various numerical parameters. Since the main objective of that section is the mass and orbital evolution of an embedded planet, we present here quantitative comparisons of planetary masses and orbital radii as function of time.

A.1. A Resolution Test

For purposes of a resolution study, we performed a three-dimensional calculation in which the grid resolution is raised by a factor of $3/2$ over the standard resolution (see section 3) in each coordinate direction, throughout the entire disk domain, and on all grid levels. Note that such an increase implies an overall refinement gain of a factor $(3/2)^3 \simeq 3.4$, in terms of *volume* resolution of the system or number of grid elements. Nested grids cover extended disk regions, so that the planet always remains in the domain described by the most refined grid during the calculation. We focus on the disk model with initial surface density at the planet's initial position $\Sigma_p = 9 \times 10^{-4} M_s a_0^{-2}$ (300 g cm^{-2}), $H/r = 0.05$, and $\nu = 1 \times 10^{-5} a_0^2 \Omega_0$. The planet's mass and orbital radius evolution, obtained at standard grid resolution, are shown in Figure 3 (*dashed curve*) and Figure 11 (*top-most solid curve*), respectively. In order to carry out a quantitative comparison, results (for both M_p and a) from the two calculations, which will be labelled as 1 and 2, are averaged over time intervals of half of the (initial) orbital period and then relative differences are computed as

$$\frac{\Delta X}{\bar{X}} = 2 \left(\frac{X_1 - X_2}{X_1 + X_2} \right), \quad (\text{A1})$$

where X is either M_p or a . In order to give time-averaged estimates of the relative differences, over the course the calculations, we perform a running-time average of quantity $\Delta X/\bar{X}$, which is defined by

$$\left\langle \frac{\Delta X}{\bar{X}} \right\rangle_t = \frac{1}{t} \int_0^t \frac{\Delta X}{\bar{X}} dt'. \quad (\text{A2})$$

Results are shown in the left panels of Figure 21. The largest differences are observed in the results for the mass evolution (*top-left*), after the onset of the rapid accretion phase (see *dashed line* in Fig. 3). The average difference, over the entire evolution, stays within 10–15%. The average relative difference between the evolution results of the orbital radii (*bottom-left*) is much smaller and remains well within 1%.

In order to test whether the orbital evolution is consistent with Type I migration theory of Tanaka et al. (2002) at our standard resolution, we set up a three-dimensional disk model with a planet that grows at a *prescribed* rate and

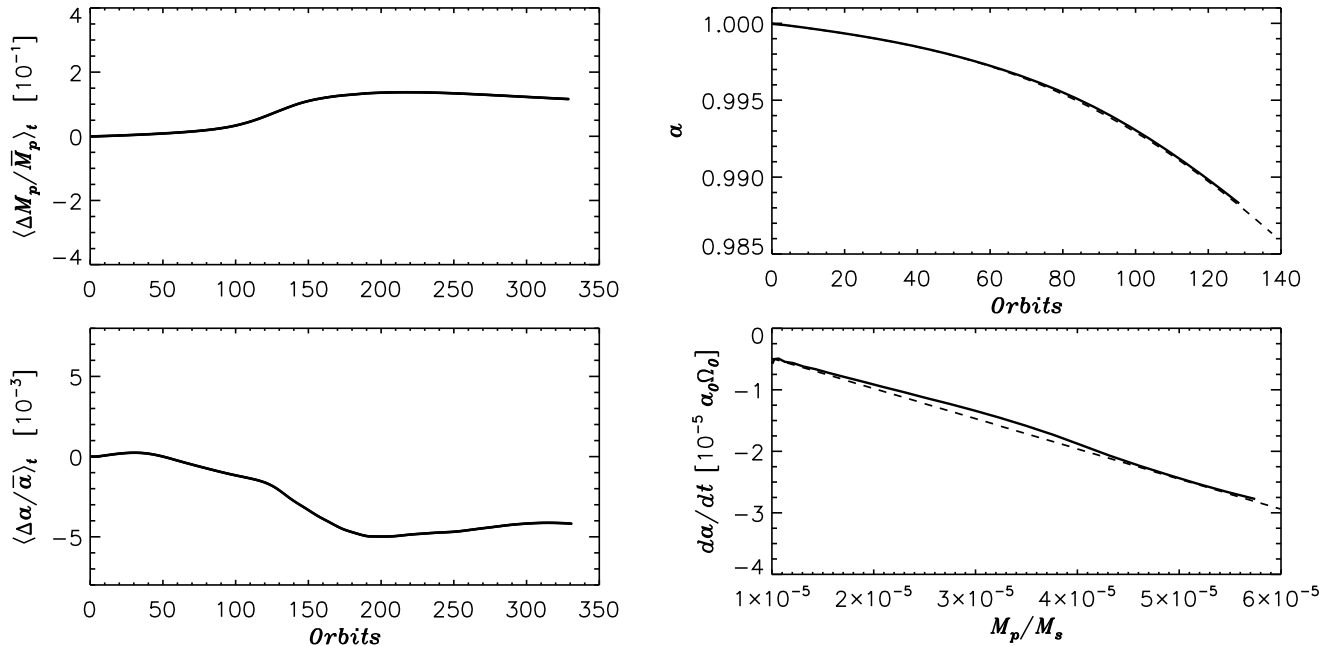


FIG. 21.— *Left*: Running-time average, defined by equation (A2), of the relative differences between two three-dimensional calculations, whose numerical resolutions differ by a factor of 3.4 in terms of grid elements (see text for details). Most of the difference in the mass growth of the planet (*top*) is accumulated between about 100 and 150 orbits, during the early phases of the rapid mass growth, when $M_p \sim 1 \times 10^{-4}$ (see *dashed curve* in Fig. 3). Overall, the running-time average of $\Delta M_p / \bar{M}_p$ is in the range 10–15%. Relative differences between the evolution of the orbital radii (*bottom*) remain negligible over the course of the calculations and the running-time average is contained within 1%. *Right*: Orbital migration of a planet that grows at a prescribed rate in a three-dimensional disk whose initial (unperturbed) surface density has slope $s = -d \ln \Sigma_p / d \ln a = 3/2$. Results from a calculation (*solid curve*) are compared to predictions of Type I theory (*dashed curve*, see section 3.2.1). The top panel shows the orbital radius evolution, whereas the bottom panel shows the migration rate as a function of the planet mass.

whose initial mass is $M_p = 1 \times 10^{-5} M_s$ (about $3 M_E$). The initial (unperturbed) surface density has slope $s = 3/2$, so that $\dot{a}_I(t) \propto M_p(t)$. In the right panels of Figure 21, results from the simulation (*solid line*) are compared against predictions of Type I theory (*dashed line*, see section 3.2.1) for both the orbital radius evolution (*top panel*) and the migration rate as a function of M_p (*bottom panel*).

A.2. Boundary Condition Effects

Boundary conditions may play some role and affect the late stages of the system’s evolution, especially when M_p becomes on the order of a Jupiter mass. In our situation, the major concerns that may arise are related to the positions of the grid radial boundaries. The finite extent of the inner radius of the grid (R_{\min}) may lead to an augmented depletion of the disk within the orbit of the planet. At the outer radial boundary (R_{\max}), reflection of waves may affect torques exerted on the planet. The first effect can be mitigated by reducing the inner radius of the grid or adopting nonreflective boundary conditions (e.g., Godon 1996, 1997), whereas the second can be largely suppressed by choosing $R_{\max} \gg a$. However, while increasing the outer grid radius possibly lengthens the computing time only because a larger number of grid elements in the radial direction is required (for a given value of ΔR), decreasing the inner grid radius directly affects the time-step of the calculation, which is proportional to $R_{\min}^{3/2}$ because of the stability criterion imposed by the Courant-Friedrichs-Lewy condition.

The left panels of Figure 22 shows a comparison of results obtained from a three-dimensional calculation ($\Sigma_p = 9 \times 10^{-4} M_s a_0^{-2}$ at $t = 0$, $H/r = 0.05$, and $\nu = 1 \times 10^{-5} a_0^2 \Omega_0$) with nonreflective boundary conditions at $R_{\min} = 0.4 a_0$ and one with $R_{\min} = 0.19 a_0$ but outflow boundary conditions, as outlined in section 2.1.3. The position of the inner grid boundary affects the density distribution interior to the planet’s orbit. The effect on the planet’s mass is at the 3% level, on average over the entire course of the simulation (*top-left panel*). The orbital radius evolution (*bottom-left panel*) displays average relative differences much smaller than 1%. In the right panels of Figure 22, results from a three-dimensional calculation with outer grid radius at $R_{\max} = 2.5 a_0$ are compared to those from a calculation in which $R_{\max} = 4.9 a_0$. Both the evolution of planet mass (*top-right panel*) and orbital radius (*bottom-right panel*) are hardly affected by the position of the outer grid boundary.

A.3. Effects of Excluded Torques

The region of space in which material is gravitationally bound to the planet depends on several disk parameters (including H/r and ν) and on the planet’s mass. Calculations with fixed mass and fixed orbit planets indicate that, for $H/r \approx 0.05$ and $\nu \approx 1 \times 10^{-5} a_0^2 \Omega_0$, only material within about $0.3 R_H$ is gravitationally bound to the planet when $5 M_E \lesssim M_p \lesssim 40 M_E$ (Hubickyj et al. 2007). Analytical and numerical models of disk formation around a Jupiter-mass

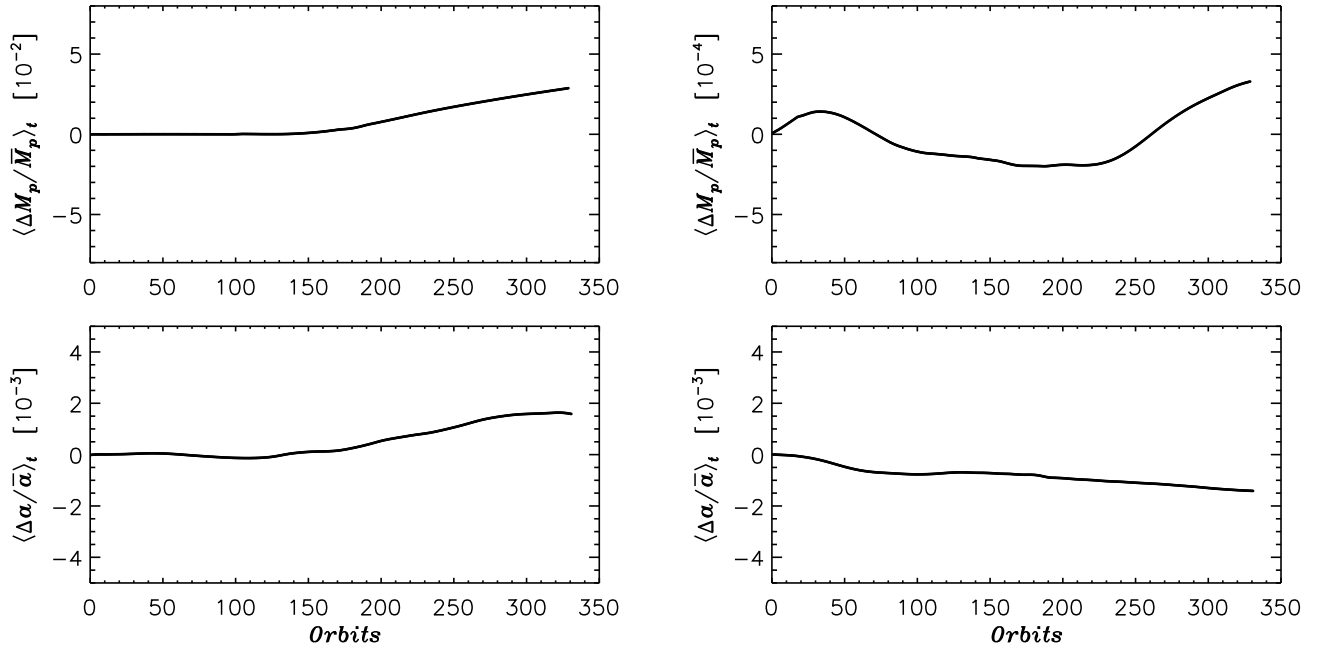


FIG. 22.— *Left*: Running-time average of relative differences between results obtained from two three-dimensional models: one with inner grid boundary at radius $R_{\min} = 0.4 a_0$ and nonreflecting boundary conditions (Godon 1996, 1997) and the other with $R_{\min} = 0.19 a_0$ and outflow boundary conditions (see section 2.1.3). Average relative differences in planet’s mass (*top*) and orbital radius evolution (*bottom*) are around 3% and $\ll \sim 1\%$, respectively. *Right*: Same comparison between two three-dimensional calculations with outer grid boundary at radii $R_{\max} = 2.5 a_0$ and $4.9 a_0$, respectively. Relative differences much smaller than 1% are observed in the evolution of both the planet’s mass and orbital radius.

planet suggest that such disks may extend over a distance of about $R_H/4$ (or less) around the planet. In the calculations presented in section 3 and 4, torques originating within $R_H/2$ of the planet are not taken into account, which may include nonzero net torques exerted by unbound material. In order to estimate how this choice affects the evolution of the orbital radius, we also considered cases in which only torques from within $0.3 R_H$ are neglected. The models with initial surface density $\Sigma_p = 3 \times 10^{-4} M_s a_0^{-2}$ and $9 \times 10^{-4} M_s a_0^{-2}$ at $r = a_0$ ($H/r = 0.05$, $\nu = 1 \times 10^{-5} a_0^2 \Omega_0$), discussed in sections 3.1.2 and 3.2.2, are restarted at regular time intervals, covering entirely their respective mass range. The evolution is then integrated for time periods of $\gtrsim 100$ orbits at each restart. We compare the evolution of orbital radii by measuring the relative differences $\Delta a/\bar{a}$ and find that for none of the cases considered $|\Delta a/\bar{a}|$ exceeds 1%. We therefore conclude that excluded torques from unbound material have only marginal effects on the results presented in section 3.2 and 4.1.

B. MIGRATION IN HIGH VISCOSITY DISKS

Results presented in section 3.2 indicate that the orbital radius evolution of a growing planet can be described reasonably well in terms of standard Type I and Type II regimes of migration (as long as the local disk mass is comparable or larger than the planet’s mass). This conclusion holds when the disk’s kinematic viscosity is $\nu \sim 10^{-5} a_0^2 \Omega_0$ (see Fig. 6) as well as when $\nu \sim 10^{-4} a_0^2 \Omega_0$ (see Fig. 9), which brackets a range of α -parameters between 4×10^{-3} and 4×10^{-2} at the location of the planet. Here we present further analysis of a case with $\nu = 1 \times 10^{-4} a_0^2 \Omega_0$ and examine cases with $\nu = 5 \times 10^{-4} a_0^2 \Omega_0$ ($\alpha \sim 0.2$), which still result in a form of Type I migration modified by the perturbed surface density of the disk.

B.1. An Additional Model With $\nu = 1 \times 10^{-4} a_0^2 \Omega_0$

As anticipated in section 3.2.2, some concern may arise when the viscous timescale, $t_\nu = r^2/\nu$, at R_{\max} becomes comparable to the length of time over which the orbital evolution of the planet is calculated. However, it is unlikely that the disk’s viscous evolution at $R > R_{\max}$ has a large impact on the results displayed in Figure 9 since t_ν at $R = R_{\max}$ is more than 6 times as long as the viscous timescale at a , about 10^4 (initial) orbital periods of the planet. Therefore, at this viscosity level, we may experience some effects only over simulations covering timescales longer than 10^4 orbits (note that inward migration will increase even further this timescale).

In order to address this issue more in detail, we set up a three-dimensional model with $\nu = 1 \times 10^{-4} a_0^2 \Omega_0$ and $H/r = 0.05$. We adopt the same parameters, numerical resolution (0.014 a_0 of linear base resolution and $9 \times 10^{-4} a_0$ of resolution in the coorbital region around the planet), and boundary conditions, as those of the simulations discussed in section 3. In this model, however, the grid radial boundary extends out to $R_{\max} = 6.7 a_0$. Therefore, the viscous timescale at R_{\max} is a factor of at least $6.7^2 \simeq 45$ as long as t_ν at the orbital radius of the planet. Thus, we could in principle follow the planet’s orbital evolution for tens of local viscous timescales. Additionally, to monitor the sensitivity of our results to boundary and initial conditions at R_{\min} , we use the initial surface density represented

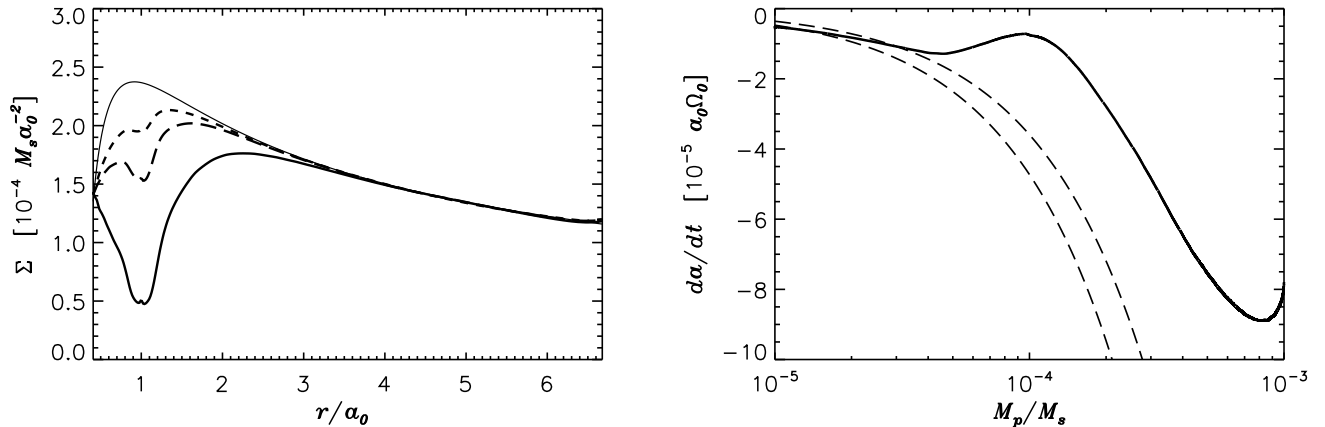


FIG. 23.— *Left*: Azimuthally averaged surface density of a three-dimensional disk with $\nu = 1 \times 10^{-4} a_0^2 \Omega_0$ and $H/r = 0.05$ at time $t = 0$ (thinner solid line) and at times when $M_p = M_p(t)$ is equal to $0.1 M_J$ (short-dashed line), $0.3 M_J$ (long-dashed line), and $1 M_J$ (thicker solid line). *Right*: Migration rate (da/dt) as a function of the planet mass (M_p) over the first 330 orbital periods of the simulation, during which time the planet’s orbit is held fixed. The planet mass growth is prescribed. Migration rates are evaluated by means of Gauss perturbation equations. The upper and lower dashed curves indicate Type I migration rates predicted by equation (17) and (18), respectively.

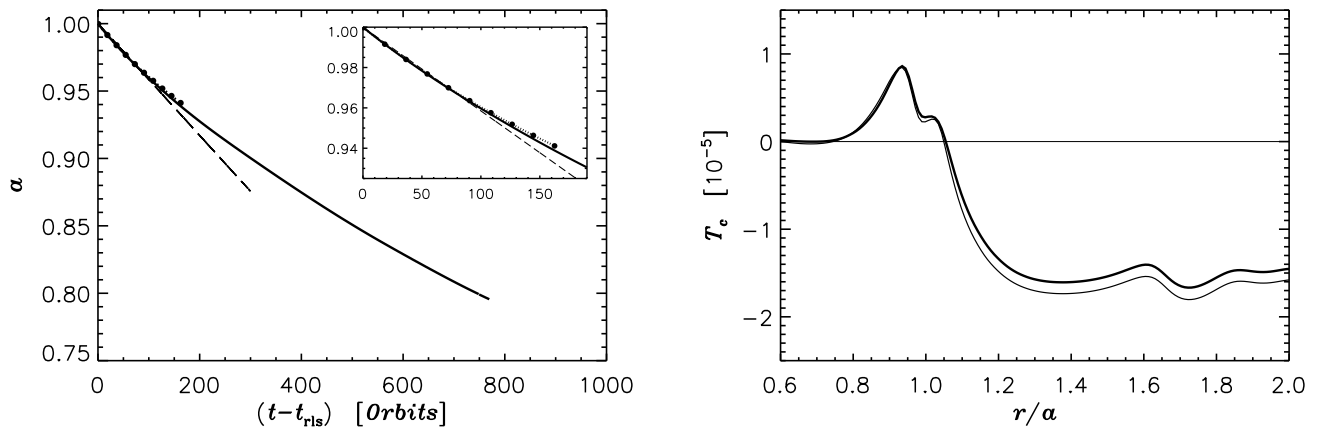


FIG. 24.— *Left*: Orbital radius evolution of a $1 M_J$ planet in a disk whose kinematic viscosity is $\nu = 1 \times 10^{-4} a_0^2 \Omega_0$ ($H/r = 0.05$). The solid line represents the model discussed in this Appendix while the dotted line with solid circles is the same as Figure 10. Note that the two models produce very similar migration tracks (see inset), although they use grids with different outer radial boundaries, respectively at $6.7 a_0$ and $2.5 a_0$, and although the surface density profiles at $r \lesssim a$ are different. In both calculations, the planet’s orbit is held fixed over the first t_{rls} (initial) orbital periods (see text for details). The dashed (straight) line has a slope about equal to $-7 \times 10^{-5} \alpha_0 \Omega_0$. *Right*: Cumulative torque at time $t = t_{\text{rls}} + 600$ initial orbital periods (thicker curve), in units of $GM_s M_p / a$, where $a = a(t)$. See text for an explanation of the thinner curve. Nearly all torque is exerted by material within a radial distance of $0.25 a$ from the planet’s orbit.

as a thin solid line in the left panel of Figure 23. The initial mass density, ρ , is related to Σ at $t = 0$ as described in section 2.1.2. Material near the planet is removed from the disk, but its mass is not added to the planet’s mass. Instead, for the purposes of this test, the planet mass is increased, at a prescribed rate, from $M_p = 1 \times 10^{-5} M_s$ ($3 M_E$) to $1 \times 10^{-3} M_s$ ($1 M_J$) over about 330 orbital periods. The orbit of the planet is held fixed ($a = a_0$) during this period of time.

The left panel of Figure 23 shows the azimuthally averaged surface density at times when $M_p = 0.1 M_J$ (short-dashed line), $0.3 M_J$ (long-dashed line), and $1 M_J$ (thick solid line). By means of Gauss perturbation equations (e.g., Beutler 2005), we measure migration rates da/dt , which result from disk’s gravitational forces (while $a = a_0$), as a function of time and hence of $M_p = M_p(t)$. The right panel of Figure 23 displays these static migration rates (solid line) compared to Type I rates (dashed curves) yielded by equation (17) and (18). The upper (lower) dashed curve refers to the unsaturated (saturated) corobital corotation torques in the linear theory (see section 3.2.1). As observed in the figure (right panel), initial migration rates agree with those predicted by linear theory. The reduction of $|\dot{a}|$, which peaks at $M_p/M_s \sim 10^{-4}$, is likely related to the onset of nonlinear effects (Masset et al. 2006).

At time $t_{\text{rls}} = 340$ orbital periods, the planet is released and allowed to change its orbit in response to disk’s torques. We recall that, at this stage, the planet’s mass is constant and equal to $1 M_J$. The migration track is displayed as a solid line in Figure 24 (left panel). The planet’s orbit is integrated for about $0.5 t_\nu$ at a_0 . The dashed (straight) line has a slope about equal to $-7 \times 10^{-5} \alpha_0 \Omega_0$ or $-0.7 \nu/a$. For comparison purposes, also plotted in the left panel of

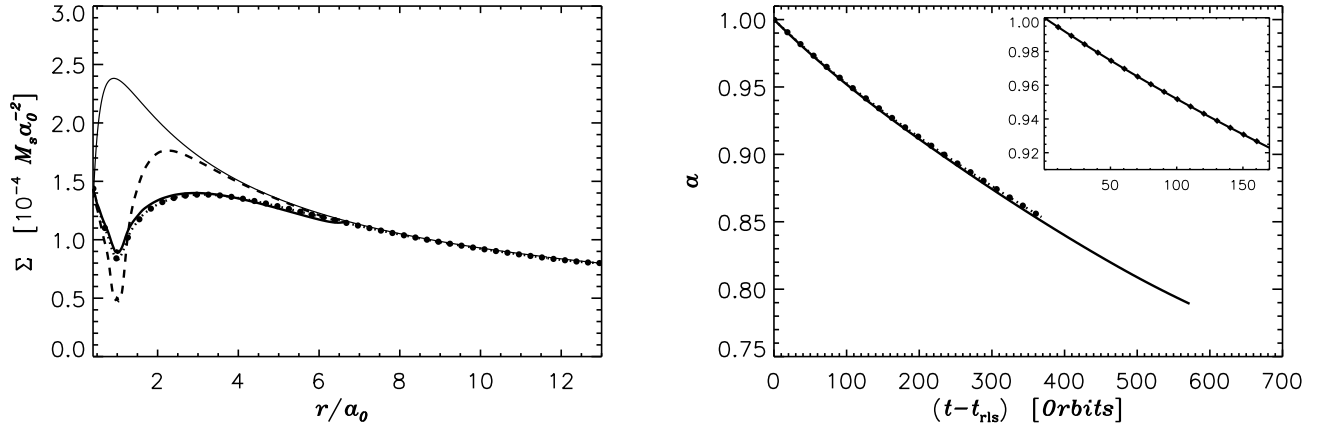


FIG. 25.— *Left*: Azimuthally averaged surface density of simulations with disk kinematic viscosity $\nu = 5 \times 10^{-4} a_0^2 \Omega_0$ and $H/r = 0.05$. The planet mass grows from $M_p \simeq 3 M_E$ to $1 M_J$, at a prescribed rate, over roughly 330 initial orbital periods. The planet’s orbit is fixed during this time interval. *Thin solid line*: Initial surface density distribution (same as the *thin solid line* in the left panel of Fig. 23). *Thick solid line*: Averaged surface density at time when $M_p = 1 M_J$ from a three-dimensional model whose outer radial boundary is $R_{\max} = 6.7 a_0$. *Dotted line with solid circles*: Averaged surface density when $M_p = 1 M_J$ from a two-dimensional model with outer radial boundary at $13 a_0$. *Dashed line*: Case of a disk with $M_p = 1 M_J$ and $\nu = 1 \times 10^{-4} a_0^2 \Omega_0$ (same as the *thick solid curve* in the left panel of Fig. 23). *Right*: Orbital radius evolution after release, $t_{\text{rls}} = 340$ initial orbits, obtained from the three-dimensional model with $R_{\max} = 6.7 a_0$ (*solid line*) and the two-dimensional model (*dotted line with solid circles*). Note that the orbital evolution covers more than 1.8 local viscous timescales. The inset shows migration tracks obtained from the three-dimensional calculations over $t_{\nu}/2$ viscous timescales at the initial orbital radius of the planet. The solid diamonds represent data from the case with $R_{\max} = 13 a_0$. The solid line represents the same model as in the main panel.

Figure 24, as a dotted line with solid circles, are results shown in the right panel of Figure 9 (*dotted line with solid circles*) and obtained with the model discussed towards the end of section 3.2.2, which has a different disk density profile inside the planet’s orbit and a different radial coverage of the disk. Despite these differences, the two models produce consistent and very similar migration tracks, indicating that disk regions at radii much smaller and much larger than the planet’s orbital radius are not playing a determinant role.

The thick curve in the right panel of Figure 24 plots the cumulative torque (in units of $GM_s M_p/a$), i.e., the torque per unit radius dT/dr integrated outward over radius, at $t = t_{\text{rls}} + 600$ orbits. As also noted for the $1 M_J$ case in Figure 2, almost all the torque is due to material within a radial distance of $0.25 a$ from the orbit of the planet. Figure 24 (*left panel*) indicates that the migration rate decreases over the course of the simulation. We find that this is not caused by a changing character of the torque per unit disk mass, dT/dM , but rather by a changing (azimuthally averaged) surface density profile around $r \sim a$. We calculate dT/dM at release time and the averaged surface density 600 orbits after release. We then use equation (20) to obtain the *expected* cumulative torque, at time $t = t_{\text{rls}} + 600$ orbits, under the assumption that the intrinsic character of dT/dM remains unchanged over time. This is plotted as a thin curve in the right panel of Figure 24, along with the *actual* cumulative torque (*thick curve*). The difference between the two curves is less than 10%.

B.2. A Model With $\nu = 5 \times 10^{-4} a_0^2 \Omega_0$

We wish to examine here whether the migration trend observed in raising the viscosity from $\nu \sim 10^{-5} a_0^2 \Omega_0$ to $\nu \sim 10^{-4} a_0^2 \Omega_0$ persists at larger viscosity. As shown in the left panel of Figure 23 (*solid line*), when $\nu = 1 \times 10^{-4} a_0^2 \Omega_0$ a Jupiter-mass planet is able to open only a shallow gap along its orbit (there is a drop in density of about a factor 3 relative to the value just outside the gap). This is because gap opening conditions are not satisfied (see section 3.2.2). At larger disk viscosity we therefore expect an even shallower gap.

We perform two three-dimensional simulations with the same setup as that outlined above but with $\nu = 5 \times 10^{-4} a_0^2 \Omega_0$ ($\alpha = 0.2$ at $r = a_0$) and outer radial boundaries at $R_{\max} = 6.7 a_0$ and $13 a_0$, respectively. The linear base resolution is $\Delta R = a_0 \Delta \theta = a_0 \Delta \phi = 0.014 a_0$ while the resolution in the coorbital region around the planet is $9 \times 10^{-4} a_0$. The viscous diffusion timescale, t_{ν} , at $r = a_0$ is approximately 320 (initial) orbital periods whereas t_{ν} at $R_{\max} = 6.7 a_0$ is over 1.4×10^4 orbits (and 5.4×10^4 orbits at $R_{\max} = 13 a_0$). We also consider a two-dimensional version of such models, having the same grid structure and resolution in the r - ϕ plane, and outer grid boundary located at $r_{\max} = 13 a_0$ (nearly 68 AU from the central star). The planet mass grows, at a prescribed rate, from $M_p \simeq 3 M_E$ to $1 M_J$ over about 330 periods (which is similar to t_{ν} at the planet position), while the planet’s orbit is held fixed. The left panel of Figure 25 shows the initial surface density (*thin solid line*) and the azimuthally averaged density profile when $M_p = 1 M_J$ for the three-dimensional model with $R_{\max} = 6.7 a_0$ (*thick solid line*) and the two-dimensional model (*dotted line with solid circles*). As reference, the azimuthally averaged density for the case with viscosity $\nu = 1 \times 10^{-4} a_0^2 \Omega_0$ and $M_p = 1 M_J$ is also plotted as a dashed line (same as the *thick solid curve* in the left panel of Fig. 24). In the overlapping disk region, two- and three-dimensional calculations give consistent results. No significant deviations from the initial density distribution are observed at $r \gg a$.

The viscosity condition for gap opening requires that $M_p/M_s \gtrsim 0.02$ (see section 3.2.2), or $M_p \gtrsim 20 M_J$, in order for

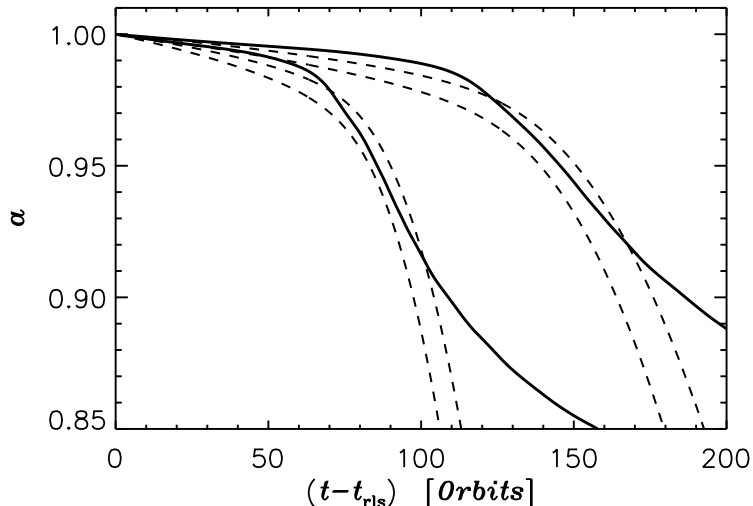


FIG. 26.— Orbital evolution under the same disk conditions as for models in Figure 11. But, the planet’s angular speed is imposed to be equal to the instantaneous keplerian value while the planet migrates in response to the nonaxisymmetric disk forces. *Solid curves*: Simulation results for orbital migration of a planet in a disk with initial surface density equal to $\Sigma_p = 9 \times 10^{-4} M_s a_0^{-2}$, or about 300 g cm^{-2} at $a_0 = 5.2 \text{ AU}$ (upper migration track), and $\Sigma_p = 1.5 \times 10^{-3} M_s a_0^{-2}$, or about 500 g cm^{-2} (lower migration track). *Dashed curves*: Predicted orbital migration according to Type I theory, equations (17) (upper curve of pair for unsaturated coorbital torques) and (18) (lower curve of pair for saturated coorbital torques). Analogous calculations executed for density distributions and disk thicknesses used in section 3 produce migration tracks that differ by $\sim 1\%$, over the entire planet mass range, from those displayed in the left panels of Figures 6, 8, and 9.

gravitational torques to overcome viscous torques. In fact, the density distribution in the left panel of Figure 25 (*thick solid line and dotted line with solid circles*) shows a form of rather shallow gap. Hence, Type II migration should not be expected.

The planet is released from its fixed orbit at time $t_{\text{rls}} = 340$ ($M_p = 1 M_J$ for $t \geq t_{\text{rls}}$) and the orbit is integrated for $1.8 t_\nu$ viscous timescales at $r = a_0$. Figure 25, (*right panel*) displays the orbital radius evolution for the two-dimensional (*dotted line with solid circles*) and three-dimensional (*thick solid line*) simulations. The two migration tracks in the main panel closely follow one other. A comparison between the results obtained from the three-dimensional models, over $t_\nu/2$ at the initial orbital radius of the planet, is shown in the inset. Again, there is no indication that disk’s evolution at $r \gg a$ has a significant influence on planet’s migration. As for the case discussed above, nearly all the torque is accumulated by material within a radial band $|r - a| \lesssim 0.25 a$ centered on the planet’s orbit.

The rate of migration after release time is approximately $-8 \times 10^{-5} a_0 \Omega_0$, which is similar to that of the solid curve in the left panel of Figure 24. This near equality is expected for Type I migration, since it is independent of the level of disk viscosity. We use the torque per unit disk mass, dT/dM , at $t = t_{\text{rls}}$ from the model with $\nu = 1 \times 10^{-4} a_0^2 \Omega_0$ discussed above in Appendix B.1 and the averaged surface density profile in the left panel of Figure 25 (*thick solid line*). By applying equation (20), we estimate the total torque expected under the assumption that dT/dM has similar shapes in the two models. There will be some dependence of $dT(r)/dM$ on viscosity, since viscosity affects the resonance widths. This estimate yields a migration rate that agrees within a factor of 1.7 with the value stated above, indicating that the intrinsic character of the torque per unit disk mass is roughly similar in these two cases.

C. CORRECTIONS FOR DISK GRAVITY

As discussed in section 4.1, there is a possible artificial torque that can act on a planet surrounded by a massive disk, when the planet responds to the gravity of the disk but the disk self-gravity is not included (Pierens & Huré 2005). This torque is a consequence of the disk’s axisymmetric gravitational force in changing the planet’s orbital rotation rate, but not changing the disk’s rotation rate (since the disk is not self-gravitating). This artificial difference leads to a shift in disk resonances that in turn leads to an artificial increase in the planet’s inward migration. It can largely be remedied by forcing the planet to rotate at the local keplerian rate, i.e., at the same speed as the gas rotates apart from effects of gas pressure. In this prescription, the planet responds to the nonaxisymmetric forces of the disk that result in migration, while undergoing orbital motion at the keplerian rate. This scheme is in reasonable accord with simulations that include the full effects of disk self-gravity (Baruteau & Masset 2008). The full effects of self-gravity cause a slightly faster migration rate than this approximation suggests. We have carried out three-dimensional simulations with such imposed keplerian planetary orbits for various disk mass cases discussed in sections 3 and 4. For mass distributions and disk thicknesses, as those applied in section 3, migration tracks show negligible differences, over the entire planet mass range. The only cases that produce changes beyond a few percent in migration rates are those in Section 4. In Figure 26 we plot the resulting migration for the same disk models as in Figure 11. The migration rates are slower, as found by Baruteau & Masset (2008). But, they are still in approximate agreement with the predictions of migration

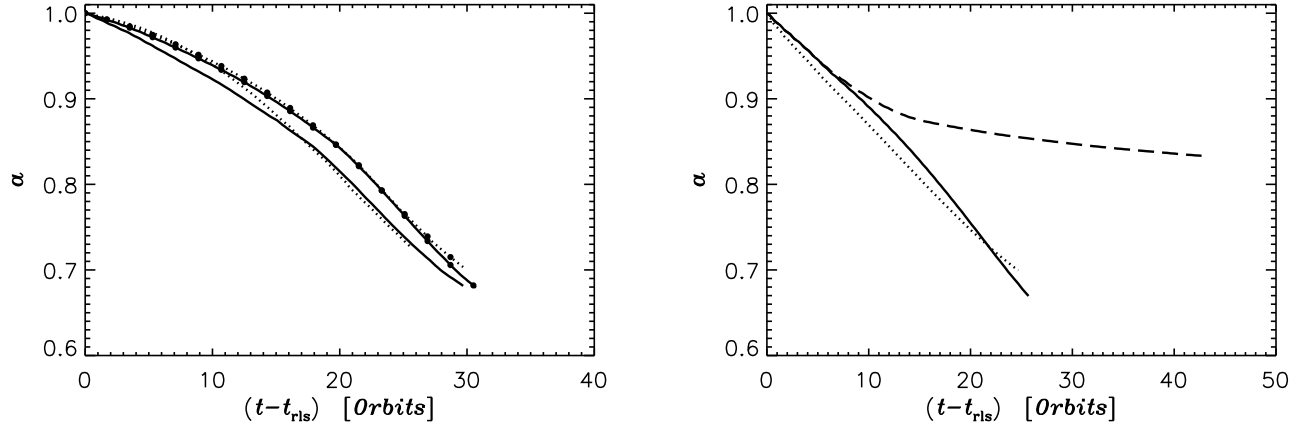


FIG. 27.— Orbital migration of a $0.3 M_J$ planet in a cold and massive disk (see section 4.3 for details). The planet’s orbit is held fixed for t_{rls} initial orbital periods. *Left*: Comparison between two-dimensional models with (*solid lines*) and without (*dotted lines*) accreting boundary conditions near the fixed mass planet ($t_{\text{rls}} = 100$). The curves marked with solid circles represent migration tracks obtained by excluding torques from within the planet’s Hill sphere. *Right*: Migration tracks from three-dimensional models with sudden release ($t_{\text{rls}} = 1$), and fixed (*solid and dotted lines*) and variable (*dashed line*) mass planets. The solid and dotted curves are for an accreting and nonaccreting planet, respectively. The long-dashed curve represents a case in which the initial planet mass ($0.3 M_J$) is augmented by the mass of the gas within $R_H/4$ of the planet.

theory.

D. ADDITIONAL TESTS ON FAST MIGRATION

Simulations of the orbital evolution of a fixed Saturn-mass planet ($M_p = 0.3 M_J$) in a cold ($H/r = 0.03$) and massive disk ($\Sigma_p = 2 \times 10^{-3} M_s a_0^{-2} \approx 670 \text{ g cm}^{-2}$ at the planet’s initial orbital radius) can lead to a buildup of gas within the planet’s Hill sphere, which is eventually halted when a sufficiently large pressure gradient is established. The mass of material that accumulates around the planet can exceed the planet’s mass, with possible effects on migration rates. In order to prevent the accumulation of gas within the Hill sphere, in the models presented in section 4.3, we applied accreting boundary conditions near the planet, without adding the gas mass to the planet mass. In this Appendix we wish to reconsider the nonaccreting configuration (as in MP03 and DBL05). The nonaccreting approach may be considered to be crudely simulating a case where some process prevents the planet from gaining further mass.

In the left panel of Figure 27, migration tracks from a two-dimensional model with an accreting planet (*solid curves*) are compared to those obtained from a two-dimensional model with a nonaccreting planet (*dotted curves*). The gas masses within the Hill spheres are drastically different: $\sim 0.07 M_p$ and $\sim 1.6 M_p$ in the accreting and nonaccreting planet cases, respectively. In the nonaccreting case, the mass of the gas ($\sim 1 M_p$) within the bound region (see Fig. 29, *right panel*) should be added to the inertial mass of the planet, thereby slowing migration (Papaloizou et al. 2007). This effect is indeed seen at early times (less than 10 orbits after release). The migration of the nonaccreting planet with bound gas (*dotted curve*) is slowed by about a factor of 2 relative to the accreting case (*solid curve*). At later times, the migration rates are closer, although it is not clear why. The reason may be related to our determination that the mass of “bound” gas decreases at later times in the nonaccreting case (see also right panel of Fig. 29).

The left panel of Figure 27 also plots the orbital evolution when torques from within the Hill sphere are not taken into account (*solid and dotted curves with solid circles*). The similarity of these migration tracks to the other plotted in the figure indicates that torques from gas in this region do not dominate the migration rates in this particular case.

In the nonaccreting case, dense gas that accumulates around the planet could be thought of as forming an envelope, once it becomes bound to the planet. A massive envelope would then participate in both the gravitational and inertial mass of the planet. We set up a three-dimensional model, with the same disk properties mentioned above (see section 4.3.1 for details), and planet mass $M_p = M_c + M_e$, where $M_c = 0.3 M_J$ is a “core” mass and $M_e = M_e(t)$ is the mass of the gas within $R_H/4$ of the planet. Given the large initial mass in the coorbital region ($\sim 2 M_J$), the planet rapidly gains mass, growing beyond $1 M_J$ in less than 25 initial orbits. The planet is released in a smooth disk after a few orbits. The orbital radius evolution is shown as a dashed line in the right panel of Figure 27, together with those from three-dimensional models with a fixed mass planet and accreting (*solid line*) and nonaccreting (*dotted line*) boundary conditions near the planet. The initial migration rates are similar in all three configurations but migration starts to rapidly slow down when the planet mass, in dashed-line case, grows beyond $M_p \approx 0.8 M_J$. This behavior resembles that seen in Figure 13 (*dotted line with solid circles*).

Figure 28 displays numerical convergence tests for the accreting (*left*) and nonaccreting (*right*) planet models presented in the left panel of Figure 27. The two simulations in the left panel have coarsest (linear) resolutions in the coorbital region that differ by a factor of 4, in both radial and azimuthal directions. Calculations in the right panel have resolutions in the coorbital region around the planet that differ by a factor of 2 in each direction.

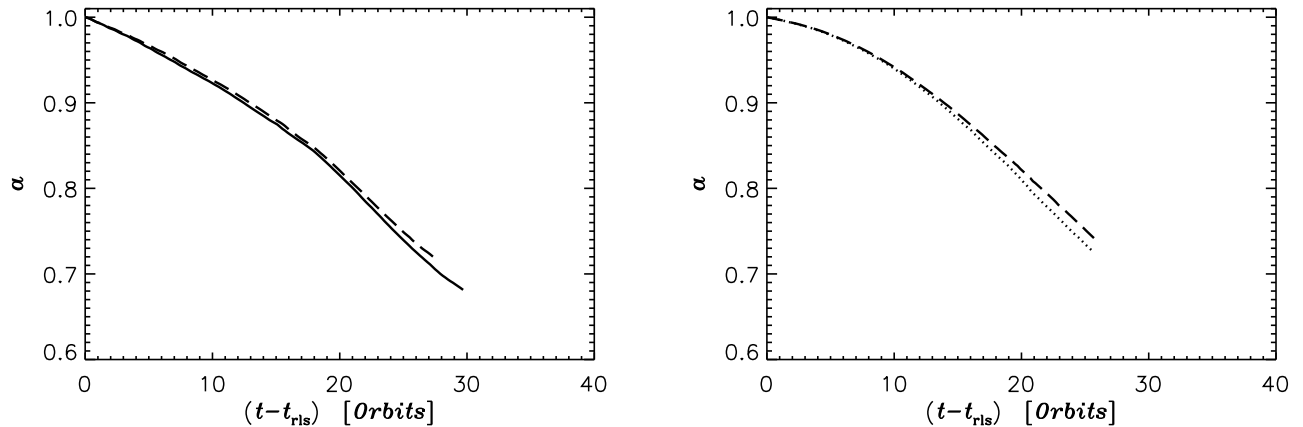


FIG. 28.— Numerical convergence tests for two-dimensional models with and without accreting boundary conditions near the planet (see Fig. 27). The planet’s orbit remains fixed for $t_{\text{rls}} = 100$ initial orbital periods. *Left:* Comparison between simulations with an accreting planet and coarsest grid resolution in the coorbital region $\Delta r = a_0 \Delta \phi = 0.014 a_0$ (dashed curve) and 3.5×10^{-3} (solid curve). *Right:* Comparison between models with a nonaccreting planet and a linear resolution in the coorbital region around the planet of $0.02 R_{\text{H}}$ (dotted curve) and $0.01 R_{\text{H}}$ (dashed curve).

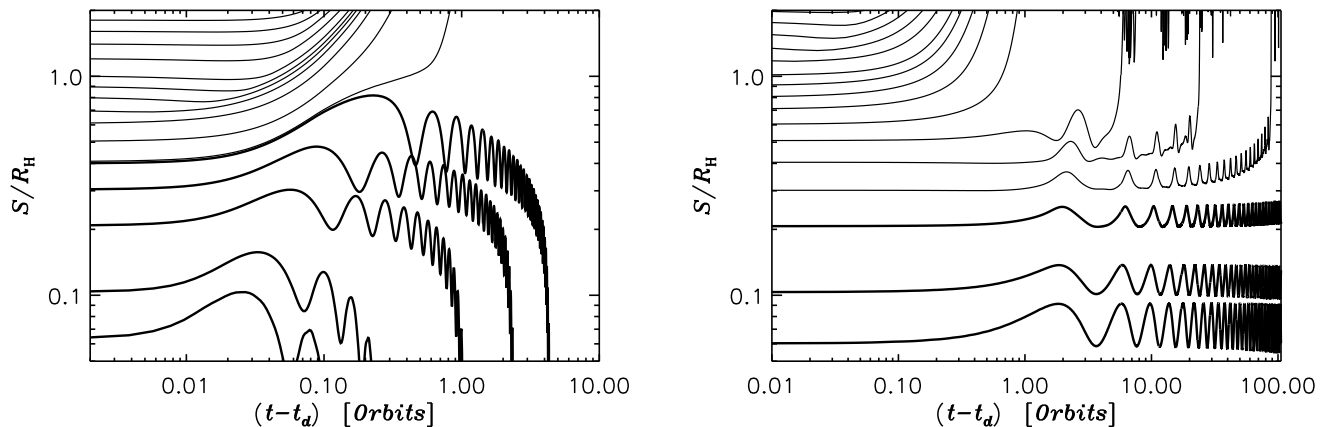


FIG. 29.— Tracer particles deployed within about $2 R_{\text{H}}$ of a $0.3 M_{\text{J}}$ planet orbiting in the cold disk model ($H/r = 0.03$) discussed in this Appendix and in section 4.3. The plot shows the distance, in units of R_{H} , from an accreting (left) and nonaccreting (right) planet. Distances of trajectories that return to the disk are indicated as thin lines, otherwise they are indicated as a thick lines.

D.1. Gas Bound to the Planet

In the calculations with an accreting planet, torque contributions from within $R_{\text{H}}/2$ of the planet are ignored. By following fluid paths, here we show that most of this material is captured and eventually accreted by the planet.

In a nonstationary flow, streamlines can be used as a proxy for fluid trajectories only over short distances and periods of time. Therefore, we track trajectories of fluid parcels by deploying tracer (massless) particles in the flow and then following their motion. This procedure allows us to obtain a reliable determination of fluid paths regardless of whether the flow is close or far from steady state.

The equations of motion of each particle are integrated every hydro-dynamical time-step by interpolating the velocity field at the particle’s location and by advancing its position in time via a second-order Runge-Kutta method. Both spatial and temporal interpolations are performed by using the velocity field with the highest resolution available, i.e., that belonging to the most refined grid level in which the particle resides. The spatial interpolation is based on a monotonized harmonic mean (van Leer 1977), which is second-order accurate and capable of handling discontinuities and shock conditions. Hence, trajectories are formally second-order accurate in both space and time.

Here we employ tracer particles to estimate the size to the region occupied by gas bound to nonmigrating planets. Tracers are deployed in the disk within about $2 R_{\text{H}}$ of a Saturn-mass planet ($M_p = 0.3 M_{\text{J}}$). We use both models with and without accreting boundary conditions near the planet discussed in this Appendix (Fig. 27, left panel) and in section 4.3. Figure 29 shows the distance from the planet, S , of particles as a function of time. Tracers are deployed at a time t_d , when the mass within the Hill sphere has reached a nearly steady value. The distance along the trajectories is normalized to the Hill radius, R_{H} . The left panel refers to the accreting planet case, whereas the right panel refers to the nonaccreting planet case. Thin curves mark distances of trajectories that are not captured and thus return

to the disk. Thick curves mark distances of trajectories that are captured in the planet's gravitational potential (*left panel*) or otherwise remain within $R_H/2$ of the planet, over the simulated evolution (*right panel*). In the accreting case, bound trajectories rapidly decay towards the planet and it is therefore possible to make a clear distinction between bound and unbound trajectories. In the nonaccreting case, the distinction is less clear and may apply only over a given amount of time.

REFERENCES

- Alibert, Y., Mordasini, C., Benz, W., & Winisdoerffer, C. 2005, *A&A*, 434, 343 [18](#)
- Artymowicz, P. 1993, *ApJ*, 419, 155 [3](#)
- Artymowicz, P. 2004, in *KITP Conference: Planet Formation: Terrestrial and Extra Solar* [8](#), [17](#)
- Baruteau, C., & Masset, F. 2008, *ApJ*, 678, 483 [10](#), [23](#)
- Bate, M. R., Lubow, S. H., Ogilvie, G. I., & Miller, K. A. 2003, *MNRAS*, 341, 213 [1](#), [2](#), [3](#), [7](#), [18](#)
- Beutler, G. 2005, *Methods of celestial mechanics. Vol. I: Physical, mathematical, and numerical principles (Methods of celestial mechanics. Vol. I / Gerhard Beutler. In cooperation with Leos Mervart and Andreas Verdun. Astronomy and Astrophysics Library. Berlin: Springer, ISBN 3-540-40749-9, 2005, XVI, 464 pp. 99 figures, 11 in color, 32 tables and a CD-ROM.)* [21](#)
- Blandford, R. D., & Payne, D. G. 1982, *MNRAS*, 199, 883 [18](#)
- Bodenheimer, P., & Pollack, J. B. 1986, *Icarus*, 67, 391 [1](#)
- Bryden, G., Chen, X., Lin, D. N. C., Nelson, R. P., & Papaloizou, J. C. B. 1999, *ApJ*, 514, 344 [7](#)
- Butler, R. P., Wright, J. T., Marcy, G. W., Fischer, D. A., Vogt, S. S., Tinney, C. G., Jones, H. R. A., Carter, B. D., Johnson, J. A., McCarthy, C., & Penny, A. J. 2006, *ApJ*, 646, 505 [2](#), [17](#)
- D'Angelo, G., Bate, M. R., & Lubow, S. H. 2005, *MNRAS*, 358, 316 (DBL05) [1](#)
- D'Angelo, G., Henning, T., & Kley, W. 2002, *A&A*, 385, 647 [2](#)
- D'Angelo, G., Kley, W., & Henning, T. 2003, *ApJ*, 586, 540 [1](#), [2](#), [7](#), [18](#)
- D'Angelo, G., Lubow, S. H., & Bate, M. R. 2006, *ApJ*, 652, 1698 [1](#)
- Dobbs-Dixon, I., Li, S. L., & Lin, D. N. C. 2007, *ApJ*, 660, 791 [2](#), [17](#)
- Eggleton, P. P. 1983, *ApJ*, 268, 368 [7](#)
- Fendt, C. 2003, *A&A*, 411, 623 [18](#)
- Flaherty, K. M., & Muzerolle, J. 2008, *AJ*, 135, 966 [17](#)
- Godon, P. 1996, *MNRAS*, 282, 1107 [19](#), [20](#)
- . 1997, *ApJ*, 480, 329 [19](#), [20](#)
- Goldreich, P., & Tremaine, S. 1979, *ApJ*, 233, 857 [15](#)
- . 1980, *ApJ*, 241, 425 [2](#), [3](#)
- Guillot, T. 2005, *Annual Review of Earth and Planetary Sciences*, 33, 493 [18](#)
- Haisch, K. E., Lada, E. A., & Lada, C. J. 2001, *ApJ*, 553, L153 [17](#)
- Hartmann, L., Calvet, N., Gullbring, E., & D'Alessio, P. 1998, *ApJ*, 495, 385 [17](#)
- Hourigan, K., & Ward, W. R. 1984, *Icarus*, 60, 29 [14](#)
- Hubickyj, O., Bodenheimer, P., & Lissauer, J. J. 2005, *Icarus*, 179, 415 [1](#), [5](#), [17](#)
- Hubickyj, O., Lissauer, J. J., D'Angelo, G., & Bodenheimer, P. 2007, *AGU Fall Meeting Abstracts*, A6 [19](#)
- Kley, W. 1999, *MNRAS*, 303, 696 [7](#)
- Li, H., Li, S., Koller, J., Wendroff, B. B., Liska, R., Orban, C. M., Liang, E. P. T., & Lin, D. N. C. 2005, *ApJ*, 624, 1003 [1](#)
- Lin, D. N. C., & Papaloizou, J. 1986, *ApJ*, 309, 846 [1](#), [8](#)
- Lin, D. N. C., & Papaloizou, J. C. B. 1993, in *Protostars and Planets III*, 749–835 [2](#), [9](#)
- Lissauer, J. J., & Stevenson, D. J. 2007, in *Protostars and Planets V*, ed. B. Reipurth, D. Jewitt, & K. Keil, 591–606 [18](#)
- Lubow, S. H., & D'Angelo, G. 2006, *ApJ*, 641, 526 [7](#), [17](#), [18](#)
- Lubow, S. H., Seibert, M., & Artymowicz, P. 1999, *ApJ*, 526, 1001 [2](#), [3](#), [18](#)
- Marcy, G., Butler, R. P., Fischer, D., Vogt, S., Wright, J. T., Tinney, C. G., & Jones, H. R. A. 2005, *Progress of Theoretical Physics Supplement*, 158, 24 [2](#)
- Masset, F. S., D'Angelo, G., & Kley, W. 2006, *ApJ*, 652, 730 [8](#), [21](#)
- Masset, F. S., & Papaloizou, J. C. B. 2003, *ApJ*, 588, 494 (MP03) [1](#)
- Mihalas, D., & Weibel Mihalas, B. 1999, *Foundations of radiation hydrodynamics* (New York: Dover, 1999) [2](#)
- Nelson, A. F., & Benz, W. 2003, *ApJ*, 589, 578 [1](#)
- Nelson, R. P., Papaloizou, J. C. B., Masset, F., & Kley, W. 2000, *MNRAS*, 318, 18 [1](#)
- Ogilvie, G. I., & Lubow, S. H. 2006, *MNRAS*, 370, 784 (OL06) [1](#)
- Paczynski, B. 1971, *ARA&A*, 9, 183 [7](#)
- Papaloizou, J. C. B., Nelson, R. P., Kley, W., Masset, F. S., & Artymowicz, P. 2007, in *Protostars and Planets V*, ed. B. Reipurth, D. Jewitt, & K. Keil, 655–668 [12](#), [24](#)
- Pierens, A., & Huré, J.-M. 2005, *A&A*, 433, L37 [10](#), [23](#)
- Pollack, J. B., Hubickyj, O., Bodenheimer, P., Lissauer, J. J., Podolak, M., & Greenzweig, Y. 1996, *Icarus*, 124, 62 [1](#), [5](#)
- Pudritz, R. E., & Norman, C. A. 1986, *ApJ*, 301, 571 [18](#)
- Shu, F., Najita, J., Ostriker, E., Wilkin, F., Ruden, S., & Lizano, S. 1994, *ApJ*, 429, 781 [18](#)
- Tanaka, H., Takeuchi, T., & Ward, W. 2002, *ApJ*, 565, 1257 [4](#), [8](#), [18](#)
- Tanigawa, T., & Watanabe, S. 2002, *ApJ*, 580, 506 [6](#)
- van Leer, B. 1977, *JCP*, 23, 276 [25](#)
- Ward, W. 1997, *Icarus*, 126, 261 [2](#), [8](#), [17](#)
- Ward, W. R. 1986, *Icarus*, 67, 164 [3](#), [4](#)
- Ward, W. R. 1992, in *Lunar and Planetary Institute Conference Abstracts, Vol. 23, Lunar and Planetary Institute Conference Abstracts*, 1491–1492 [4](#)
- Ward, W. R., & Hourigan, K. 1989, *ApJ*, 347, 490 [14](#)
- Wuchterl, G. 1991, *Icarus*, 91, 53 [1](#)
- . 1993, *Icarus*, 106, 323 [5](#)
- Yuan, C., & Cassen, P. 1994, *ApJ*, 437, 338 [4](#)
- Zhou, J.-L., & Lin, D. N. C. 2007, *ApJ*, 666, 447 [18](#)
- Ziegler, U., & Yorke, H. W. 1997, *Computer Physics Communications*, 101, 54 [2](#)